Empirical and computational study of vasculogenesis

Ph.D. Thesis

András Szabó
Department of Biological Physics,
Eötvös Loránd University, Budapest

Advisor:
András Czirók
PhD, associate professor

Graduate School of Physics
Doctoral Program for Statistical Physics, Biological Physics and Quantum Systems

Head of School: Prof. Dr. Zalán Horváth, regular member of HAS
Head of Program: Prof. Dr. Jenő Kürti, D.Sc.

2011

Contents

1. Introduction 5
   - 1.1. Cell motility 7
   - 1.2. Vasculogenesis 12
   - 1.3. Models of vasculogenesis 15
   - 1.4. Cell based models 20
2. Methods 25
   - 2.1. Empirical methods 25
   - 2.2. Image processing 27
   - 2.3. Cell trajectory analysis 29
3. Network formation in cell culture 35
   - 3.1. Empirical findings 35
   - 3.2. The preferential attraction model 40
   - 3.3. Interacting particle model 41
   - 3.4. Preferential adhesion in the cellular Potts model 48
   - 3.5. Discussion 57
4. Cell streaming in monolayer cultures 61
   - 4.1. Empirical findings 62
   - 4.2. Self-propelled cellular Potts model 70
   - 4.3. Discussion 78
5. Multicellular sprout formation 83
   - 5.1. Empirical findings 84
   - 5.2. Self-propelled cellular Potts model with tip cells 86
   - 5.3. Discussion 95
6. Summary 99
7. Összefoglalás 101

Acknowledgement

First, I would like to thank my advisor, András Czirók, for all the help and mentoring throughout the years. Looking back on the time we have worked together, I feel extraordinary lucky to have met him, and feel grateful for all the knowledge and enthusiasm he has passed on to me since then.

I would like to thank the work of my colleagues, Edina Kósa, Renáta Ünnep and Előd Méhes at the Eötvös University and the support of the people at the Department.

The inspiring discussions with Charles Little, Brenda Rongish, the work with Anastasiia Aleksandrova, Paul Rupp and the help of Tracy Cheuvront and Mike Filla have all contributed momentum for the completition of this work.

Last, but not least, I thank for the support and patience of my whole family and friends.

1. Introduction

The accelerating technical development enabled science to expand with an unprecedented rate. New tools for acquiring knowledge resulted in a huge amount of raw data to be interpreted and analyzed, especially in biological sciences. One role of biological physics is to help process and interpret these new findings. Biophysicists face problems at various length-scales, from understanding the conformation changes in molecules to the collective motion of several hundreds of animals.

At the cellular level, the interaction of macromolecules or other sub-cellular components is a lively research area. Cell behavior emerges as the result of such interactions and although the main cellular components are well known, the connection between the sub-cellular and cellular behavior is often obscure. Both molecular and cell biology can benefit from the use of modeling when testing hypotheses explaining the emergence of cellular function. The collective behavior of several cells is, perhaps, another step further from understanding, and the long-term goal is to understand embryonic development.

During development, the structures in the body arise from smaller-scale participants through either local interactions and self-organization, or by a genetic preset program. A good example of such a genetic hard-wiring are the HoX genes responsible for the patterning of the head-tail axis, including vertebral column segmentation [82, 74]. HoX genes are located in the genome in a strictly defined sequence and are expressed in this order during body-axis formation. This way they define, for instance, segmentation of the hindbrain and the vertebrae, or in drosophila, the body segments of the insect. Several experiments showed, that when a HoX gene is knocked out, the corresponding body part is missing from the animal causing severe to lethal deficiencies (see for example Lufkin et al. [51], Mark et al. [55], Chisaka and Capecchi [8]). These systems are more rigid compared to the self-organized ones, where the rules encoding the pattern are embedded in each individual sub-component and the emerging structure is the result of a collective behavior.

Vasculogenesis, the emergence of a vascular network in warm blooded animals, is one of the problems in developmental biology where our understanding

seems to be within reach: it occurs in a relatively simple anatomical environment and involves only a single cell type. Besides being a candidate model system for understanding cellular self-organization, the vascular network is of fundamental medical and biological importance: it is functional even before it is completed and it's rearrangement (angiogenesis) carries on throughout life. The vasculature is one of the most dynamic organs in warm blooded animals.

The focus of this work on understanding the important mechanisms and cell-level behavior that gives rise to vasculogenesis. The outline is as follows: a brief overview of motile cell properties is followed by describing the vasculogenesis process. After the methods section, three major biological aspects of vasculogenesis is studied: specialized cell-cell interactions, directional persistence of cellular motion and inhomogeneity of the cell population.

In section 3. the emergence of multicellular networks is presented and analyzed in different biological environments. Based on the empirical evidence, a phenomenological hypothesis on cellular behavior is constructed, suggesting that cells prefer elongated neighbors or structures to round, isotropic ones. Two, widely applied cell-level models are introduced to test the behavior of such cells. The emergence of network-like structures in even these simple models is in good agreement with the observations, although some aspects are not satisfying. An important feature, sprout formation, has a time course substantially different from the experiments.

Section 4. deals with one of the most important cellular feature missing from the simple models presented in the previous section. Self-propulsion of endothelial cells is studied in high density cultures, where cellular streams are apparent. These few cells wide and tens of cells long streams form and disappear at random positions, creating vortices. Neighboring streams often move in opposite directions, creating regions with high shear or "shear-lines". Implementing a coupled system of cell polarity and self-propulsion in one of the above models readily reproduces the streams.

Sprouting is studied in detail in section 5.. Based on biological observations, a motile cell with a large persistence length is distinguished in the model. Sprouts are formed by this "leader" cell pulling others from a cell aggregate. Applying the preferential attachment hypothesis for the cells, realistic sprouts are reproduced.

With this complete model the most important observed features of vasculogenesis, and network formation in general, are described.

1.1. Cell motility

In this study the behavior of individual cells is modeled. A brief summary of the relevant biological aspects is provided in this section.

Cells are self-contained living units that metabolize and reproduce, and are covered by a lipid membrane that acts as a two-dimensional fluid layer [81]. The mechanical stability of cells is provided by three scaffolding systems within the cell: the actin, microtubule (MT) and intermediate filamental systems, that together make up the cytoskeleton. Although the exact role of the individual systems is not yet clear, the actin and MT scaffolds are important in cell motion, besides their many other functions, such as signaling or trafficking within the cell. Both systems are made up of long polymer filaments that are constantly being re-generated through an active, energy consuming process. The plasticity of the cytoskeleton is controlled by the rate of synthesis and de-polymerization of these filaments.

Microtubules are stiff cylinders built from tubulin dimers, radially organized in the cell by the microtubule organizing center (or MTOC), located near the cell nucleus (fig. 1). The actin system is built up of flexible polymers (filamental actin) of (globular) actin monomers (fig. 2). Under certain circumstances, the filaments may be organized in highly ordered, parallel bundles, and are used to construct stress fibers (through the activity of Rho proteins) or long poles, filopodia, for exploring the surrounding environment. The other typical form of actin is a brush-like mesh, called lamellipodia, used for creating wide, highly fluctuating lobes in front of the moving cell. This spatially extended form is created by branches forking off the filaments, seeded by the Arp2/3 protein complex.

Physical contact and force-transduction towards the environment is created through adhesion complexes: macromolecular structures anchored in the cell's membrane. The active adhesion sites are connected to the cytoskeleton through adaptor molecules within the cell, and to the sites of other cells or certain extracellular molecules, on the outside. The molecular constitution of these sites defines

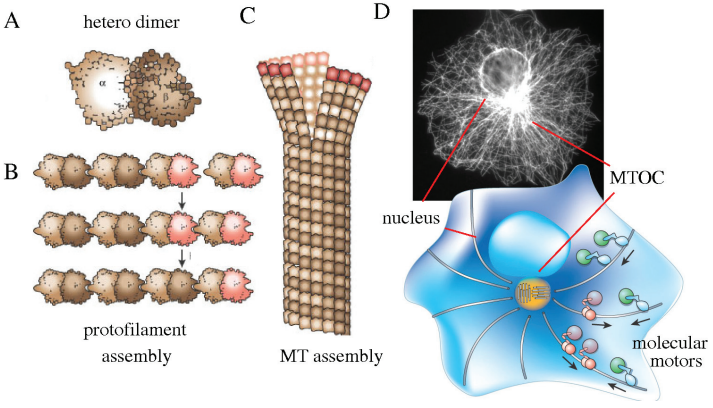

Figure 1: Microtubules are polymerized from tubulin hetero-dimer proteins (A). The dimers attach together in protofilaments (B) that form cylinders, called microtubules (C). These stiff tubes are organized centrally by the microtubule organizing center (MTOC), normally located near the nucleus (D). Besides other functions, microtubules provide mechanical stability and intracellular transport with the help of associated motor proteins. Image from Howard and Hyman [40].

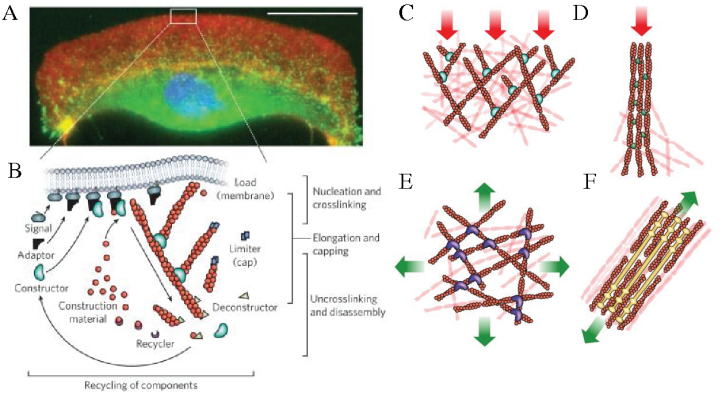

Figure 2: Filamental actin (F-actin) is polymerized from globular actin (G-actin) monomers. Actin plays a crucial role in pushing the cell membrane forward at the leading edge: panel A shows actin (red) accumulation at the front of a cell. In this region, F-actin is mainly organized into a space filling brush-like structure (B and C). Branching is initiated by the Arp2/3 complex and the polymerization is controlled through blocking by caps, de-polymerization and recycling free G-actin by recycler molecules. Actin can be organized into different forms: at the leading edge, the brush-like structure (C) resists compression (red arrows) and parallel fibers (D) constitute long filopodia; under the cell membrane, "cortical" actin filaments are crosslinked into an isotropic mesh (E) surrounding the whole cell, to carry load (green arrows) in all directions uniformly; filaments in parallel bundles inside the cell coupled with myosin motor protein structures (F) are able to conduct forces generated by the actin-linked myosin motor proteins. Image from Fletcher and Mullins [20].

their function, for instance: cadherins are transmembrane proteins typically connecting two cells, integrins typically anchor a cell to a specific peptide (RGD) in the extracellular matrix (ECM). The ECM is a heterogeneous, interconnected mesh of macromolecular chains produced and assembled by the cells. One of the main functions of the ECM is to provide a scaffold for movement, but it also plays an important role in directing and signaling cells. Its physical and signaling properties are set by its biochemical composition.

Besides adhesion sites, other cellular contacts are present that serve as an information channel: specific ligands binding to their cell-surface receptors can initiate several complex mechanisms within the cell, triggering responses ranging from the change in the electric potential to the production of new proteins or even cell death. This way cells are able to respond to their environment, by for example initiating movement towards higher concentrations of certain molecules (chemotaxis) or stiffer environments, substrates (durotaxis).

Cell movement is a complex and highly regulated action. The forces for displacing the cell body are created by myosins pulling actin filaments relative to each other in stress fibers that are anchored between adhesion sites (fig. 3) [48]. This contractile force pulls the environment through the adhesion sites and creates the traction force. The forward movement of the cell membrane is thought to be activated by the small GTPase complex, Rac1, at the leading edge, by activating the Arp2/3 complex to provide new actin nucleation sites. The Rac1-Arp2/3 cascade eventually results in a local increase in actin polymerization, pushing the plasma membrane forward to create a lamellipodium [53, 75]. In the newly formed lamellipodium, new adhesion sites attach to the environment and are connected to the cytoskeleton. In the rear of the cells, adhesions sites are dismantled and the cell body is de-attached from the surroundings by the pull of the stress fibers.

The frontal growth area and the rear, where adhesion sites have to be decomposed, are clearly distinguished by their biochemical composition [71, 75]; in other words: the cell is polarized. It is not yet clear, however, what is the exact molecular mechanism for this process: the best documented front - rear polarization mechanisms involve either the mutual inhibition of Rac and Rho activity [75, 61], and/or the accumulation and segregation of the phosphatidyl-inositol

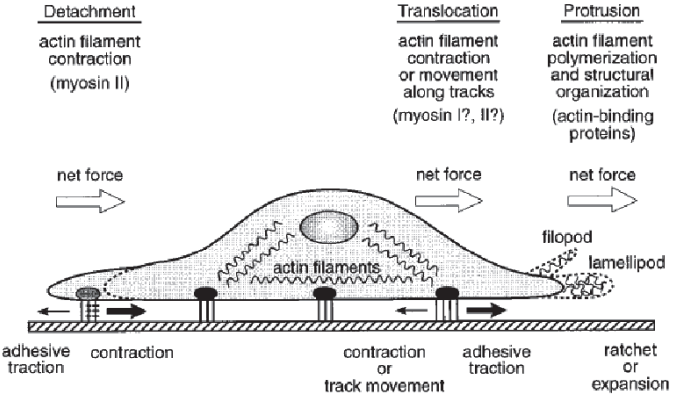

Figure 3: Cell motion is accomplished by the coordination of several processes: membrane protrusions through enhanced actin polymerization and new adhesions forming at the front, stress fibers providing tension in the cell body, and detachment of adhesion at the rear. Image from Lauffenburger and Horwitz [48].

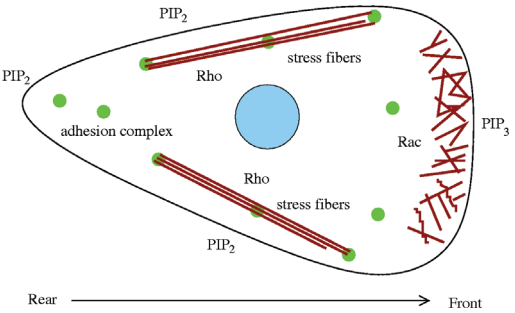

Figure 4: Biochemical composition of the front and rear of a moving cell differs. At the front of the cell, PIP_3 is accumulated in the membrane and high levels of active Rac result in the increase of actin polymerization. At the rear and sides of the cell, PIP_2 is present in the membrane and stress fibers are formed as a result of Rho activity. Adhesion complexes form on the front and de-attach at the rear.

PIP_2 and PIP_3 components in the cell membrane [53, 30] (fig. 4). Through positive feedback loops, both the Rac/Rho and PIP_2/PIP_3 systems are able to amplify slight spatial differences in upstream inputs and even develop a spontaneous polarity [53, 30]. This amplification of presumably random receptor activity and the related spontaneous symmetry breaking could explain the onset of spontaneous cell motility in a homogeneous environment.

1.2. Vasculogenesis

In warm blooded animals, the vasculature is formed at an early stage of embryo development, in a region, where only three cellular layers are present. First a polygonal network of endothelial cells, the primary vascular plexus is formed (fig. 5), which later evolves and continuously adapts to meet the ever-changing demands of the organism, throughout a lifetime. The role of the vasculature is not only to serve the metabolic needs of other organs and tissues, but also to enhance communication between distant parts of the body by convecting signaling molecules or even cells.

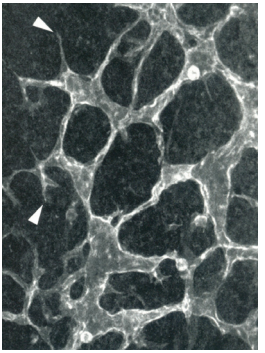

Figure 5: Primary capillary plexus in the quail embryo, the first network formed by endothelial cells. Arrowheads indicate sprout tips. Image from Drake and Little [15].

The emergence of the primary vascular network from individual cells or cell clusters is termed vasculogenesis. The network spans the whole of the embryo and connects to the outer source of nutrients, be it the vasculature of the mother, or the yolk of the egg. However large the network may be, in warm blooded animals vasculogenesis is now thought to be a self-organized pattern of the endothelial cells, in opposition with the pre-patterned or genetically programmed patterning observed for example in zebrafish [103].

The process is studied in various animal models, including mouse and birds (chicken and quail). Bird embryos are experimentally more accessible and due to the discovery of a QH1 antibody [70], the quail model became a frequently used one. The QH1 antibody specifically binds to a cell surface epitope on endothelial cells of the quail, making it possible to follow the emerging vasculature by immuno-staining.

Vasculogenesis takes place after gastrulation, when the top germlayer penetrates the space between the two epithelial sheets through the primitive streak (fig. 6), creating a middle layer, the mesoderm. The central region of the mesoderm gives rise to the (intra-) embryonic tissue, whereas tissue outside of this

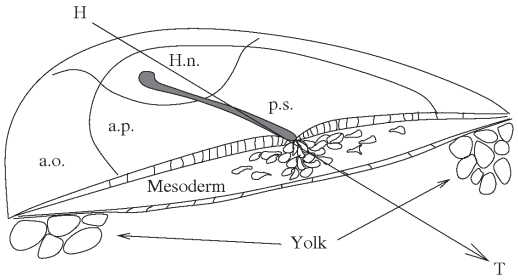

Figure 6: The anatomy of the bird embryo just before the onset of vasculogenesis. The embryo consists of three disk-shaped germ layers, with the upper and lower two enclosing the middle mesoderm, where the vasculature will emerge. The outer rim of the disk is in contact with the underlying yolk and is named area opaca (a.o.) after its opaque quality. The embryo itself is forming in the center region of the disks, the area pellucida (a.p., clear window), where the layers are separated from the yolk. The mesoderm is formed by cells entering into the space between the endoderm and epiblast through the primitive streak (p.s.), a process called gastrulation. At the end of the primitive streak towards the future head (marked by H) a specialized region forms, called Hensen's node (H.n.). This region is shifting towards the future tail (T) on the body axis and somites are formed in its wake, that will give rise to vertebrae among other structures. During this movement, vasculogenesis takes place on the two sides of the streak.

region is referred to as the extraembryonic. The two regions are optically distinct under the microscope and are named area pellucida (clear window, intraembryonic) and area opaca (opaque window, extraembryonic) (fig. 7). Both regions form vascular networks but typically in two different ways: in the extraembryonic region precursor cells differentiate in cell-aggregates (blood-islands), and form the network by mainly sprouting; in the intraembryonic part, however, no blood-islands are seen, but individual cells emerge that connect into a network. Networks of the two regions fuse and later give rise to the embryonic blood-current that transports nutrients from the yolk to the embryo.

The robustness of the patterning process is demonstrated by the high level of similarity between the primary networks formed in different specimen. This

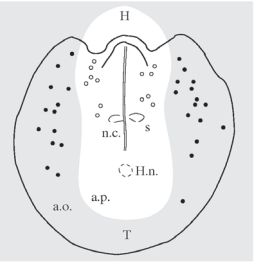

Figure 7: A sketch of the pre-vascular bird embryo, viewed from the ventral (belly) side. The embryo consist of three germ layers, circular in shape, with the mid-line (notochord, n.c.) marking the body axis from the future head (H) to the future tail (T), ending in the Hensen's node (H.n.). In the intraembryonic (area pellucida, a.p., white area), individual endothelial cells appear (open dots), whereas in the area opaca (a.o., gray areas) blood islands form (filled dots). The first air of somites are indicated (S).

similarity would imply the guidance of a hard-wired pre-pattern but the networks are only statistically similar on a large scale, and nearly always differ on smaller scales. The pre-pattern hypothesis can be excluded based on chick and quail graft experiments of Poole and Coffin [73]: after a portion of one embryo is transplanted into an other region of a different embryo, cells adapt to their surroundings and assimilate into their new environment. Since the whole tissue has been transplanted, we can exclude the genetic hard wiring as well as the environmental pre-pattern hypothesis and assume a cell-level mechanism for self-organization behind the process.

1.3. Models of vasculogenesis

Several attempts have been made to explain the emergence of the primary plexus, from the early reaction-diffusion hypothesis of Alan Turing [93] to more sophisticated models. With the development of the experimental techniques new, refined models were constructed, focusing on the mechanisms suggested by the observations. In turn, models can help to stimulate questions of high importance for better

understanding and suggest new experiments.

Technically, models for vasculogenesis can be divided into two main groups: continuum and cell-based models. Continuum models describe cells in terms of cell-density, with a dynamics specified by partial differential equations. One strength of these models is that they can be treated analytically, as well as with simulations. In cell-based models, cells are represented by one or more discrete entities and the dynamics is defined by rules imposed on them. The discrete entities may represent a whole cell, or a fraction of the cell, but do not necessarily carry any specific biological function. These fractions typically represent a volume fraction of a cell, as in for example the cellular Potts [33] or the subcellular element model [66], but another recent model uses area-segments of the cell-surface as subdivisions [6].

Depending on the scale of the phenomena to be modeled, both the continuum or the agent-based model types might be valid to describe the mature vasculature. In vasculogenesis, however, the forming pattern includes small details, comparable to the cell size: the forming branches of the network are only a few cells wide. Vasculogenesis is therefore on the verge of validity of continuous description. Due to the rapid growth in computational power, recent models of vasculogenesis are utilizing the discrete, cell based description of cells.

Chemotaxis models

It is known that most motile cells react to concentration gradients of certain molecules such as growth factors, generally referred to as chemoattractants. The mechanism is called chemotaxis. Even a slight difference in the concentration along the cell perimeter can guide a cell towards the direction of higher concentration [36, 30]. Tumor cells, for instance, support their growing metabolic needs by producing chemoattractants to attract sprouts from nearby vessels.

One of the most widespread models used for vasculogenesis is the chemotaxis driven assembly. The main idea of this model is that cells are attracted by the concentration gradient of a diffusing substance that is produced by the cells at a certain rate. This substance provides the means to a long-range interaction through which cells are able to navigate towards each other.

A formulation of the chemotaxis model for vasculogenesis is given by Gamba et al. [29], where cells are represented by cell density $n(\mathbf{r}, t)$, a continuous function, and velocities of the cells is given by the velocity field $\mathbf{v}(\mathbf{r}, t)$. The concentration of the chemoattractant is represented by $c(\mathbf{r}, t)$. The model assumes that (i) cells are moving in the direction of the chemoattractant's concentration gradient, (ii) cells secrete the chemoattractant at a constant rate and (iii) the chemoattractant diffuses and decays with constant rates. Formally:

$$\frac{\partial n}{\partial t} + \Delta(n\mathbf{v}) = 0, \tag{1.1}$$

$$\frac{\partial \mathbf{v}}{\partial t} + \mathbf{v}(\nabla \mathbf{v}) = \kappa \nabla c, \tag{1.2}$$

$$\frac{\partial c}{\partial t} = \mu \nabla^2 c + \alpha n - \tau^{-1} c, \tag{1.3}$$

where the strength of chemotactic response is given by κ, and μ, α and τ are the diffusion coefficient, the production rate and the characteristic decay time of the chemoattractant, respectively. Initiated from homogeneous cell distribution, polygonal networks of cells emerge (fig. 8). The system is adaptive, but the characteristic size of the network continuously grows until reaching the final state: one, compact cell aggregate.

A cell-based chemotaxis model was suggested by Merks et al. [58], based on the cellular Potts model of Graner and Glazier [33]. In this two-dimensional model (i) cells have an elastically pre-defined area and cell length, (ii) produce a chemoattractant, (iii) move in the gradient direction of the chemotactic field, which (iv) diffuses and decays with a constant rate. Here, cell elongation defines the emerging pattern morphology: round cells simply form aggregates, whereas elongated cells connect into a network. Thus, it seems, the final state of the chemotactic models is different in discrete models, where an additional length scale is introduced in the dynamics.

Cells in these networks, however, seem to be under compression. The concentration gradient of the chemoattractant at the interface of cell clusters drives cells inward and compresses the cluster. This process is balanced by the elastic compressibility rule and is apparent from cell areas consistently below the equilibrium value. The pressure creates an instability at the aggregate surface and results in

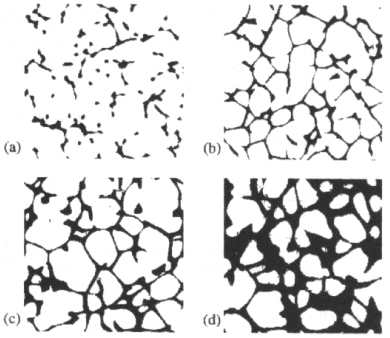

Figure 8: Networks formed in the continuous chemotactic model of Gamba et al. [29]. Initiating the model from homogeneous cell distribution, cellular networks emerge at different cell densities: 50 (a), 100 (b), 200 (c) and 400 (d) cells/mm^2. Figure from Gamba et al. [29].

jets of cells erupting from the aggregate, providing biologically unrealistic sprouting.

Another version of the chemotactic models inhibits chemotactic activity on cell-cell contact surfaces [59]. The model is based on the same cellular Potts model, but the cell length constraint is dropped. Cells in the model do not react to the chemoattractant gradient, if they contact a neighbor cell in that direction. The biological basis for this contact inhibition rule is the lack of filopodial extensions on the contact surface of two cells. In this model, initially scattered cells connect into a regular polygonal network with well defined pattern size.

Mechanical model

The observation, that cell aggregates pull on their substrate led to the development of a mechanical model for vasculogenesis and cellular network formation in general [54]. The model is based on the Murray-Oster mechanochemical theory [63, 68], according to which cells are exerting traction force on the underlying deformable substrate and are allowed to proliferate or die and produce different

molecules affecting their behavior.

In the mechanical model for vasculogenesis [54], only the mechanical aspect of the Murray-Oster theory is kept, thus cells exert forces on the substrate and displace it together with other cells. This minimal mechanism creates networks very similar to the ones produced by in vitro cells cultured on soft substrates. Substrate malleability and traction strength of cells are crucial for the patterning process.

The model has been further developed by Namy et al. [65]: cells actively migrate in the direction of substrate gradients, a property called haptotaxis. In this model the mechanical properties of the substrate are better fitted to the experimentally used gels and pattern formation occurs even without significantly displacing the substrate.

Although the emerging networks are reminiscent of the observed ones, experimental evidence shows that during formation, the cell-sprouts are not necessarily growing directly towards each other [77], which contradicts the purely mechanical idea. Another contradicting factor is that cellular networks are able to form on rigid substrates as well, suggesting that at least another mechanism is responsible for this phenomenon.

A phenomenological model

A new approach to modeling vasculogenesis is presented in this study. Experimental observations led to the assumption that cell motility is enhanced by the close contact with elongated cellular structures. Hence, a model is constructed in which cells preferentially attach to their elongated neighbors. In this model, sprouts are initiated from the adhesive cluster of cells by either random, or persistent movement of individual cells. Due to cellular adhesion, sprout leaders assume an elongated shape and thus attract more cells into the forming sprout. As shown later, under certain circumstances the assumption proves to be sufficient for initiating and maintaining sprouts, leading to network formation.

1.4. Cell based models

Particle model

When modeling cells, a simple model is beneficial for better understanding the mechanisms acting in the background of its overall, phenomenological behavior and therefore easing the comparison with real life. Probably the simplest way to model moving objects is to represent them with points. When describing a cell, a convenient choice to represent its position is with the cell's center of mass and its apparent total speed by a vector. The model is defined by the equations describing the motion of the individual objects and the interaction between them. The interaction may involve pairwise attraction, repulsion or, for example, interaction between the velocities. Usually, these interactions are represented as pair-interactions and the net effect on a cell is the sum of the pair-interactions. These effects can technically be handled as effective forces acting on the objects. The forces, however, do not need to be actual, physical forces, they rather express movement probabilities, since cell motion is definitely not a passive response to external force.

The motion of the objects is iterated in discrete time-steps by calculating every object's new position and velocity; for object i:

$$\mathbf{r}_i(t+1) = \mathbf{v}_i(t)\Delta t \qquad \mathbf{v}_i(t+1) = \sum_j \mathbf{f}_{i,j}\Delta t \tag{1.4}$$

where $\mathbf{r}_i(t)$ is the position, $\mathbf{v}_i(t)$ is the velocity of object i, Δt is the discrete time-step and $\mathbf{f}_{i,j}$ is the effective interaction between the objects i and j. The summation may involve all objects in globally interacting models.

To describe cells, the dynamics can be transformed to produce a stochastic, persistent diffusion process presented in eq. 2.4. A similar model aiming to describe chemotacting cells is presented by Stokes et al. [85], where cells interact with a concentration gradient as well. Transforming the chemotactic interaction to describe general cellular interaction, the evolution of velocity is then written as

$$\mathbf{v}_i(t+\Delta t) = -\frac{\mathbf{v}_i(t)}{\tau}\Delta t + \frac{\sqrt{2\mu}}{\tau}\xi + \sum_j \mathbf{f}_{i,j}\Delta t \tag{1.5}$$

where τ describes the persistence time of the motion, μ is a diffusion parameter and ξ is an uncorrelated noise. The coefficient of the random term is often written as $\sqrt{\alpha} = \sqrt{2\mu}/\tau$, where α represents the magnitude of random movement accelerations.

This model is free from the complexity of describing the cellular shape which makes it accessible and simple to characterize. However, in some cases it can be important to describe the shape of the cell or enumerate its immediate neighbors. For this end, the shape of the cell is usually derived from the Voronoi tessallation of the configuration: the cell is considered to have the shape of its Voronoi cell, and its contact neighbors are its Voronoi-neighbor cells.

Cellular Potts model

The cellular Potts model (CPM) was introduced by Graner and Glazier [33] to describe cell sorting with the preferential adhesion hypothesis. The Potts model is a generalization of the Ising model allowing multiple spin states. The CPM is a modification of the Potts model, designed to describe cells.

The model is defined on a lattice. In this work the model is restricted to two dimensions since the cell cultures that we model are planar as well. Cell configurations are described by the integer value function σ defined on the lattice. Cells are represented as simply connected domains, i.e., a set of adjacent lattice sites sharing the same label σ, equal to the cell index i ($0 < i \leq N$, where N is the number of cells in the simulation). The shape of the cell free areas, designated by $\sigma = 0$, is unconstrained.

Cell-cell adhesion, cell compressibility and cell boundary roughness are controlled through a target function u, that evaluates configurations as

$$u = \sum_{\mathbf{a},\mathbf{b}:|\mathbf{a}-\mathbf{b}|=1} J_{\sigma(\mathbf{a}),\sigma(\mathbf{b})} + \lambda \sum_{k=1}^{N} \delta A_k^2. \tag{1.6}$$

The first term in eq. 1.6 is a weighted sum of the length of cell-cell and cell-medium boundaries. Formally, $J(\sigma(\mathbf{a}), \sigma(\mathbf{b}))$ is a ferromagnetic interaction between adjacent spins $\sigma(\mathbf{a})$ and $\sigma(\mathbf{b})$. The summation goes over adjacent lattice

sites, and the $J_{i,j}$ interaction matrix $(0 \leq i, j \leq N)$ is given as

$$J_{i,j} = \begin{cases} 0, & \text{for } i = j \\ \alpha, & \text{for } ij > 0 \text{ and } i \neq j \text{ (cell-cell boundary)} \\ \beta, & \text{for } ij = 0 \text{ and } i \neq j \text{ (free cell boundary).} \end{cases} \tag{1.7}$$

The surface energy-like parameters α and β characterize cell-cell adhesions and cell surface fluctuations in the model. The magnitude of these values determines the roughness of cell boundaries: small magnitudes allow dynamic, long and hence curvy boundaries, while large magnitudes restrict boundaries to straight lines and thus freeze the dynamics. This correlation between measured surface energies and cell surface roughness has been elegantly demonstrated with tumor spheroids by Hegedüs et al. [38]. The parameter $2\beta - \alpha$ specifies the preference of cell-cell connections over cell-medium boundaries: free cell boundaries are penalized for $2\beta > \alpha$ [33].

The second term in eq. 1.6 is responsible for maintaining a target cell size. The deviation of the i-th cell's area from a specified target size is denoted by δA_i. Parameter λ define cell stiffness, and may depend on the measure of cell elongation to reflect assumptions that elongated cells tend to be stiffer [106].

The use of a temperature-like parameter, as rule (3) of Glazier and Graner [32], analogous to eq. 1.8 simply scales each CPM parameter α, β and λ by the temperature, a constant, therefore it is omitted in this description. When comparing this study with those that include a temperature in the simulations, the parameter values presented in this study are to be compared with the corresponding values divided by the temperature.

Cell movement consists of a series of elementary steps. Each step is an attempt to copy the label value from a randomly chosen lattice site $\mathbf{a}$ to a randomly chosen, but adjacent site $\mathbf{b}$. This elementary step is executed with a probability $p(\mathbf{a} \to \mathbf{b})$. The probability assignment rule ensures the maintenance of a target cell size and the adhesion of cells:

$$\ln p(\mathbf{a} \to \mathbf{b}) = \min[0, -\Delta u(\mathbf{a} \to \mathbf{b}) + w(\mathbf{a} \to \mathbf{b}))], \tag{1.8}$$

where u is a goal function characterizing the configurations and w is an extension introduced to contain terms directly assigned to the elementary step considered (see later). The latter allows the specification of a broader spectrum of cellular behavior and represents an extension to the original CPM of Graner and Glazier [33]. The difference $\Delta u(\mathbf{a} \rightarrow \mathbf{b})$ is obtained by evaluating u both at the current configuration and at the configuration obtained after the elementary step $\mathbf{a} \rightarrow \mathbf{b}$ has been applied. In addition, domains are required to remain simply connected after each elementary step, thus cells do not break apart or form holes.

Since updating each lattice position takes more steps in a larger system, the elementary step cannot be chosen as a unit of time. Instead, the usual choice for time unit – the Monte Carlo step (MCS) – is L^2 elementary steps, where L is the linear system size.

As the behavior of cells is in many respect dissimilar to that of the medium, a function χ is introduced to distinguish between the two:

$$\chi(x) = \begin{cases} 0, & \text{for } \sigma(x) = 0 \\ 1, & \text{elsewhere} \end{cases} \tag{1.9}$$

The models presented in this work were implemented in a suitably modified version of the open-source CPM code of Merks et al. [58], freely available from [56].

Although the CPM describes cellular motion in detail, one of its shortcomings is the lack of transparency: parameters, such as surface contact energies are hard to measure. Also, since cell level behavior is controlled through elementary steps, complex and indirect rules are needed for the formulation of certain hypotheses.

2. Methods

2.1. Empirical methods

Cell cultures

In vitro experiments with cell lines C6, C2C12, 3T3, and various endothelial cells cultured on fibronectin, Matrigel or tissue culture plastic substrates were carried out by my colleagues.

Substrates Fibronectin (Sigma) was incubated on TC plastic for 24 hours at room temperature at 10 μg/ml concentration. EHS mouse sarcoma basement membrane extract (Matrigel) was obtained from multiple sources: Becton Dickinson (Franklin Lakes, NJ, USA), R&D Systems (Minneapolis, MN, USA; sold as Cultrex Basement Membrane Extract) and Cell Biolabs Inc. (San Diego, CA, USA; sold as ECM gel, CBA200). The solutions were allowed to gel at 37 ^{o}C for 30 minutes yielding gels between 40 and 120 μm thickness.

Cells C6 glioma, C2C12 myoblast and fibroblast derived 3T3 cells were cultured in DMEM (Sigma-Aldrich) with 10% (C6, 3T3) or 15% (C2C12) fetal calf serum (Gibco, Csertex Ltd, Budapest, Hungary) at 37^oC in a 5% CO_2 atmosphere.

Bovine capillary endothelial (BCE, Veitonmaki et al. [98]) cells, primary bovine aortic endothelial cells (BAEC's) and human umbilical vein endothelial cells (HUVEC's; Lonza, Basel, Switzerland) were propagated on TC substrates and then transferred into a microscope-mounted incubator to record their motility on a variety of ECM substrates.

BAEC's were isolated from bovine aorta as described in Twal et al. [94] and cultured in M199 medium supplemented with 10% fetal bovine serum and 10 ng/ml of bFGF. For cell tracking experiments, BAEC's were cultured in serum-free, CO_2-independent medium (Leibovitz L15, Mediatech, VA, USA) supplemented with 1% Nutridoma (Becton Dickinson). Dishes were coated with Matrigel (Becton Dickinson) by mixing 1 volume of Matrigel with 3 volumes of ice-cold serum-free L-15 medium. 50 μl/cm^2 was dispensed into each well of a 24 well culture dish (Corning) and allowed to gel. Cells were added to each well

at a density of 10^5/cm^2 and allowed to attach for 2 hrs.

BCE cells were cultured in DMEM (Sigma) with 10% FCS (GIBCO) and imaged in the same medium supplemented with 40 ng/ml bFGF (Chemicon, USA), 80 nM (50 ng/ml) PMA (Sigma), and 50 μg/ml ascobic acid (Sigma). 35 mm culture dishes were coated with undiluted Matrigel (Cultrex) at 12.5 μl/cm^2 density. Cells were added to each dish at 7×10^4/cm^2 density and allowed to attach for 2 hours.

HUVEC's were grown in EGM-2 growth medium (Lonza) with 5% FCS for up to 3 passages. For cell tracking experiments, HUVEC's were cultured in the same medium supplemented with 40 ng/ml bFGF, 40 ng/ml VEGF (Pierce, Rockford, IL, USA), 80 nM PMA, and 50 μg/ml ascorbic acid. 35mm culture dishes were coated with Matrigel (Cell Biolabs) by mixing 1 volume of Matrigel with 1 volume of ice-cold PBS. 40 μl/cm^2 of the mixture was dispensed in the dishes and allowed to gel. Cells were added to each dish at 7×10^4/cm^2 density and allowed to attach for 2 hours.

Time-lapse imaging

Cells were observed in multiple fields for at least 15 hours with automated phase-contrast time-lapse microscopy, described in detail by Czirók et al. [9]. Briefly, a computer controlled, wide-field, epi-fluorescent microscope equipped with a computer controlled motorized stage records images at 1.3-0.87 μm per pixel resolution of preset fields of view at fixed, 3-10 minute intervals (values varied between different experiments). Live cell imaging is done with a microscope stage-mounted incubator, controlling the atmosphere and temperature of up to 4 petri-dishes.

To capture large-scale structures, several, neighboring fields of view are imaged with a slight overlap allowing for the alignment of the fields to create a mosaic image. The alignment is carried out by first roughly positioning the images according to the preset coordinates and then refining the positions by cross-correlation. In some cases, the consequent time-frame images were corrected for the global skew of the recorded cultures.

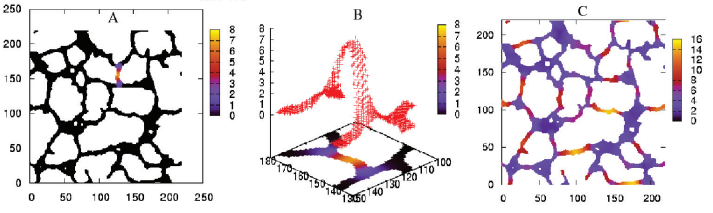

Figure 9: Measuring the local anisotropy demonstrated on a model network configuration. Concentration $c(\mathbf{r}, t)$ is diffused from various points in the segmented and smoothened images (A). The ratio of the principal momentums calculated from the resulting concentration profile (shown in (B)) is used to characterize the anisotropy of the whole area covered by $c(\mathbf{r}, t)$. The map of the whole configuration is then constructed from the individual measurements (C).

2.2. Image processing

Segmentation

For the detection of cell bodies in phase contrast images, the two stage segmentation scheme of Wu et al. [105] was used. Briefly, an approximate area enclosing the cells is selected first, based on the substantially higher brightness variation within and around the cells (see for example fig. 12a,b in section 3.). In the second step, cell bodies are located as areas darker than the bright halo surrounding phase objects. This automatic procedure is not satisfactory for the identification of individual cells as nearby cells may constitute one cluster in the segmented image, due to a possible unified halo surrounding them. The procedure, however, is sufficient for the detection of the morphology of cell-configurations.

Local anisotropy maps

Local elongation of cell configurations or structures was measured using a novel morphometric process. The segmented images are smoothened with a long-pass filter. A diffusion process is started from a point $\mathbf{r}_0$ in the image, which acts as a fixed point-source within the diffusing field $c(\mathbf{r}, t)$ (fig. 9). The brightness value

$I(\mathbf{r},t)$ of the segmented and smoothened image sets the diffusion coefficient of the process as

$$\mu(\mathbf{r},t) = \begin{cases} I(\mathbf{r},t), & \text{for } I(\mathbf{r},t) > I_{min} \\ 0, & \text{otherwise.} \end{cases}$$

Thus, the diffusion coefficient is truncated at a threshold I_{min} producing a spreading, well-defined front around the point-source. The principal moments (λ_1, λ_2 and $\lambda_1 \geq \lambda_2$) calculated from the concentration's inertia tensor are used to characterize the elongation of the local area as $A(\mathbf{r}) = \sqrt{\lambda_1/\lambda_2} - 1$. For isotropic areas $\lambda_1 \approx \lambda_2$, whereas in elongated areas $\lambda_1 > \lambda_2$. The area is grown until its width reaches a pre-defined value, the typical width of a single cell. The anisotropy value is assigned to the area covered by the particular diffusion process. By repeating the procedure for several points $\mathbf{r}_0$, the whole image can be mapped to result in a local anisotropy map.

Structure factor

The structure factor of images is used to characterize pattern size apparent in cellular configurations. Based on the $I(\mathbf{r})$ segmented image intensities, the structure factor is calculated from the spatial power spectrum $P(q)$ as

$$S(q) = \frac{P(q)}{P_1(q)} \tag{2.1}$$

where $P_1(q)$ is the form factor of single cells and $P(q)$ is the radially averaged and Hanning-windowed power spectrum of the spatial pattern $I(\mathbf{r}) \equiv I(x,y)$ as

$$P(q)\delta q = \left\langle \mathcal{F}_{2D}\left[I(x,y)\sin(\frac{\pi x}{L})\sin(\frac{\pi y}{L}) \right] \right\rangle_{q<|\mathbf{k}|<q+\delta q}, \tag{2.2}$$

where the two dimensional Fourier transformation with frequency-domain variable $\mathbf{k}$ is denoted by $\mathcal{F}_{2D}$ and $\langle ... \rangle_{q<|\mathbf{k}|<q+\delta q}$ represents a radial average. The form factor $P_1(q)$ was obtained in an analogous manner from synthetic configurations, where single cell images were re-positioned and re-oriented randomly without overlap (see fig. 12).

Time lag images

A convenient method to visualize temporal changes recorded with time-lapse microscopy is to create the time lag image or kymogram. The region of interest from each time frame is compressed to a few pixel wide – essentially one dimensional – image. The compression may be done by projecting the image onto a selected line, or simply by copying a few pixel wide stripe at a fixed position of the image sequence. The resulting slices are then montaged next to each other in chronological order. This way, movement in the movie appear as tilted lines on the kymogram. The slope of the line is defined by the speed of the original motion as one side of the kymogram represents distances in the original images and the other dimension represents time.

2.3. Cell trajectory analysis

Manual cell tracking

Cells were tracked either manually or automatically on the time-lapse recorded images. Manual tracking was carried out by marking the center position $\mathbf{r}_i(t)$ of every cell i on the recorded frames corresponding to times t.

Automatic cell tracking

For automatic cell tracking, the uneven illumination of the microscopic images were corrected by subtracting from each image the average of the whole time-sequence, using ImageJ plugins. Camera noise was reduced by applying a 3×3 pixel median filter.

The first two steps of the tracking procedure are a two-step cross-correlation displacement-prediction (PIV: particle image velocimetry), as described by Zamir et al. [108]. Briefly, the consecutive images are subdivided into tiles. A tile at time t is shifted with various vectors $\mathbf{r}$ and its cross-correlation value with the image detail at the shifted position at time $t + \Delta t$ is assigned to each vector $\mathbf{r}$. Mapping all possible values of $\mathbf{r}$ results in a function $C(\mathbf{r})$ with a maximum at the most probable displacement value. Using this prediction, a second, smaller subdivision

of the image is used to give a more precise displacement estimate with the same procedure.

In the third step, the PIV prediction is followed by a gradient search for local brightness minimum, as in phase contrast images cell nuclei are darker than the surrounding cell body. For the cell lines investigated, the estimated error rate of the procedure (mistraced cells per trajectory segments obtained) is less than 1%. For initial cell center positions we used centers of clusters obtained by a suitably chosen brightness threshold.

Cell velocities

The velocity, $\mathbf{v}_i(t)$ was calculated as the net displacement of the cell centroid during a 1 hour long time interval:

$$\mathbf{v}_i(t) = \frac{\mathbf{r}_i(t + \Delta t) - \mathbf{r}_i(t)}{\Delta t} \tag{2.3}$$

where $\Delta t = 1$h. Although experimental recordings would allow for better time-resolution, using a time-lag of 1 hour reduces the error in the position tracking. The displacement of cells during 1 hour is typically one cell-diameter and the tracking of displacements below this range are less reliable.

The persistent diffusion process

An intuitive measure of cell motion properties is the average displacement over a time-frame. Based on the temporal autocorrelation and the displacement over time functions of two dimensional cell trajectories, motion of cells is often described as a persistent diffusion process [18, 85, 79]. The simplest model for such a motion is the Ornstein Uhlenbeck (OU) process [67, 96, 19], describing the Brownian motion of non-interacting particles. In this model, the time evolution of the velocity of cell i, $\mathbf{v}_i$ can be given as:

$$\frac{d\mathbf{v}_i}{dt} = -\frac{\mathbf{v}_i}{\tau} + \sqrt{\alpha} \cdot \xi_i, \tag{2.4}$$

where τ is the characteristic persistence time and α is the magnitude of random movement accelerations. The first term on the right-hand-side describes a relaxation or decay of the velocity and the second term is responsible for the noise in the system.

Random movement is described by a white noise function $\xi_i = \xi_i(t) = d\mathbf{W}_i/dt$, the derivative of a $\mathbf{W}_i(t)$ Wiener process, and $\langle\xi\rangle = 0$, $\langle\xi_i(t) \cdot \xi_j(t')\rangle = \delta_{ij}\delta(t - t')$. Functions δ_{ij} and $\delta(t - t')$ are the Kronecker delta and Dirac delta functions, respectively.

Although α and τ fully describe the model, more intuitive parameters can be established: cell speed S is given by Doob [14] as $S = \sqrt{\alpha\tau}$. The random motility coefficient [45, 1, 85], analogous to the diffusion coefficient of Brownian particles, is

$$\mu = \frac{\alpha\tau^2}{2} = \frac{S^2\tau}{2}. \tag{2.5}$$

The average displacement squared over a time t is given by Fürth's formula [28]:

$$D^2(t) = 2S^2\tau^2\left(\frac{t}{\tau} - 1 + e^{-t/\tau}\right). \tag{2.6}$$

Thus, for short time periods cells move at a constant speed S, as the distance is proportional to the time elapsed, while the motion is diffusive when investigated over a long time frame:

$$D(t) \approx \begin{cases} \sqrt{2}St, & \text{for } t \ll \tau \\ 2\sqrt{\mu t}, & \text{for } t \gg \tau. \end{cases}$$

This function is relatively simple to measure from experimental data and gives access to the important parameter values of the OU model. Measurements performed with non-interacting endothelial cells and fibroblasts resulted τ, α and calculated speed values in the $0.1 - 5h$, $100 - 2000\mu m^2/h^3$ and $10 - 60\mu m/h$ range, respectively [85].

The above process aims to describe the motion of Brownian particles at finite temperatures. Motion of animal cells, however, is far more complex and is driven

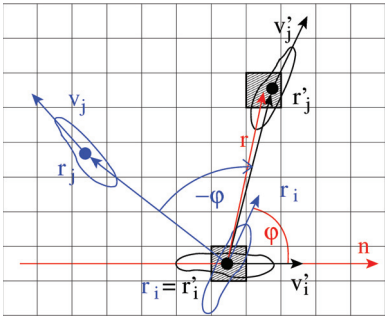

Figure 10: Calculation of the flow-field $\mathbf{V}(\mathbf{r})$. The simple, two-cell configuration at time t includes cells i and j. Their original orientation and position is marked with blue. Dots at positions $\mathbf{r}_i$ and $\mathbf{r}_j$ mark cell centers, cell velocities $\mathbf{v}_i$ and $\mathbf{v}_j$ are plotted as vectors. Cell i is heading in the direction φ (relative to an arbitrarily selected reference direction $\mathbf{n}$). To calculate the flow field around cell i, first the configuration is rotated by $-\varphi$. The center of cell j in the rotated configuration, $\mathbf{r}'_j$, falls in the vicinity of vector $\mathbf{r}$ and therefore is counted in the average $\mathbf{V}_{i,t}(\mathbf{r})$. The vicinity, $B(\mathbf{r})$ is defined as a two dimensional bin centered at the position $\mathbf{r}$. The procedure is then repeated for each cell i and $\mathbf{V}_t(\mathbf{r})$ is calculated from averaging through all cells i and j for which $\mathbf{r}'_j - \mathbf{r}_i \in B(\mathbf{r})$ holds in the rotated configuration. Finally, the $\mathbf{V}_t(\mathbf{r})$ fields are averaged through different time frames.

by an active, complex molecular machinery, therefore, parameters τ and α represent an effective value and depend substantially on the molecular state of the cells.

Flow-fields

In high density cell cultures local, anisotropic velocity patterns - streams - are observed. The usual spatial correlation of velocities averages the field cannot be used to obtain the characteristic width and length of these structures. Instead, we introduced a statistical measure, here referred to as the average flow field, $\mathbf{V}(\mathbf{r})$, that surrounds moving cells.

The velocity of cell i at time t is denoted by $\mathbf{v}_i(t)$, the direction of $\mathbf{v}_i(t)$ relative

to a fixed reference is $\varphi_i(t)$. The reference direction was arbitrarily chosen to be the positive direction of the x-axis. Flow field $\mathbf{V}(\mathbf{r})$ is calculated as

$$\mathbf{V}(\mathbf{r}) = \left\langle \mathbf{R}_{-\varphi_i(t)} \mathbf{v}_j(t) \right\rangle_{(i,j)^*,t}, \tag{2.7}$$

where $\mathbf{R}_\alpha$ is the operator for a 2D rotation with an angle α as

$$\mathbf{R}_\alpha = \begin{pmatrix} \cos\alpha & -\sin\alpha \\ \sin\alpha & \cos\alpha \end{pmatrix} \tag{2.8}$$

The $\langle ... \rangle_{(i,j)^*,t}$ average in eq. 2.7 is calculated over all possible time points t and cell pairs i, j that satisfy

$$\mathbf{r}_j(t) - \mathbf{r}_i(t) \in B(\mathbf{R}_{\varphi_i(t)}\mathbf{r}), \tag{2.9}$$

where $B(\mathbf{r})$ represents a two-dimensional, square bin with a fixed size, centered at position $\mathbf{r}$.

Practically, the vector field is shifted to locate the selected cell i in the origin and then rotated to align the velocity vector of cell i in the direction of the x-axis. The resulting shifted and rotated vector fields are calculated for all cells and time-frames, and are averaged, applying a two-dimensional bin-grid for the positions. The calculation for one cell in a simple, two-cell configuration is demonstrated on fig. 10. The resulting vector-fields are then binned and averaged over multitude and time.

Statistical errors are estimated as the standard error of the mean (SEM). SEM values are calculated from data points which we consider statistically independent. To eliminate known correlations in the velocity field we subdivide the original 2+1 dimensional velocity field data (2 spatial and 1 temporal dimensions) into non-overlapping blocks. The size of the blocks is chosen to be equal to the spatial and temporal correlation lengths of the velocities. From each block k a flow field is calculated separately, and the resulting $\mathbf{V}_k(\mathbf{r})$ fields are considered as independent. The presented $\mathbf{V}(\mathbf{r})$ fields are point-by-point averages of the corresponding $\mathbf{V}_k(\mathbf{r})$ fields, and the number of blocks is used as sample size in SEM calculations. SEM values are presented by a color code assigned to the ratio of SEM$(\mathbf{r})$

to $|\mathbf{V}(\mathbf{r})|$: the zero value is mapped to black, the unit value is mapped to yellow.

3. Network formation in cell culture

Although vasculogenesis is a prominent example of cellular network formation, several other cell types are capable of exhibiting similar behavior in culture [99]. The most common observable feature of these cultures are the emerging linear, multicellular structures that, at the right density, interconnect and give rise to a network. This sprouting phenomena was found to be an important part of vasculogenesis [77].

As described in section 1.3., the two main mechanisms proposed to explain network formation are the mechanical hypothesis, where the elasticity of the substrate plays a key role, and the autocrine chemotaxis mechanism, where a chemoattractant diffuses and creates a concentration distribution in the culture that guides patterning.

Both mechanisms may be biologically relevant, but cannot account for networks formed under certain circumstances: multicellular linear segments of various cell types are also forming when grown under normal tissue culture conditions on a solid substrate. In these experiments the rigid substrate excludes the mechanical mechanism and convection currents in the culture medium – generated by temperature inhomogeneities within the incubator and the vibrations of microscope stage motion – are expected to hamper the maintenance of concentration gradients, or impose a strong directional bias upon the chemotaxis-related cell movements. Furthermore, a specific chemotactic response is empirically unproven and unlikely to be shared by a great variety of cell types.

3.1. Empirical findings

Linear structures form on stiff substrate with convecting medium

Muscle-progenitor mouse C2C12 and rat C6 glioma cells form linear structures on rigid tissue culture plastic substrate even with a strong convection current in the culture medium (fig. 11). To measure the convection currents close to the culture surface, 0.5 μm diameter latex beads (Sigma) were immersed into the medium. Bead motion was recorded within a 20 μm thick volume above the culture surface, delimited by the field depth of the 10$\times$ microscope objective. As a representative

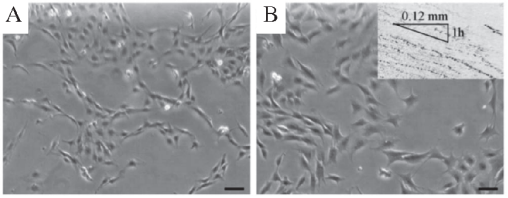

Figure 11: Linear structures form in cultures of C6 (A) and C2C12 (B) cells on rigid substrate with convecting medium. The inset shows a time-lag kymogram of the motion of latex beads in the medium. [88]

sample in fig. 11 inset demonstrates, in our experimental setup convection currents were sustained for hours with speeds exceeding 100 μm/h, an order of magnitude larger than the typical cell speed.

Multicellular linear segments form networks

Linear arrangements of multiple cells form in C6 or 3T3 fibroblast cultures when grown under standard culture conditions on a solid substrate (fig. 12a and b). The multicellular morphology is characterized statistically by the average local anisotropy as the function of local cell density (surface fraction covered). First, the cell-occupied area is identified by a segmentation procedure described in 2.2. section (fig. 12c). A measure of local anisotropy, $A(\mathbf{r})$, is then calculated as described in section 2.2.. The resulting anisotropy maps reveal the highly elongated structures (fig. 12e).

Individual cells take up a highly elongated shape in the configurations, contributing to the local anisotropy measure. To measure the contribution of multicellularity, segmented images have been randomized: images of individual cells were randomly re-oriented and re-positioned on the image without overlapping, to maintain cell density (fig. 12d). The local anisotropy of resulting synthetic images represent the contribution of the individual cell-shape to the average local anisotropy (fig. 12f).

Cell density influences the possible cell arrangements and thus the average

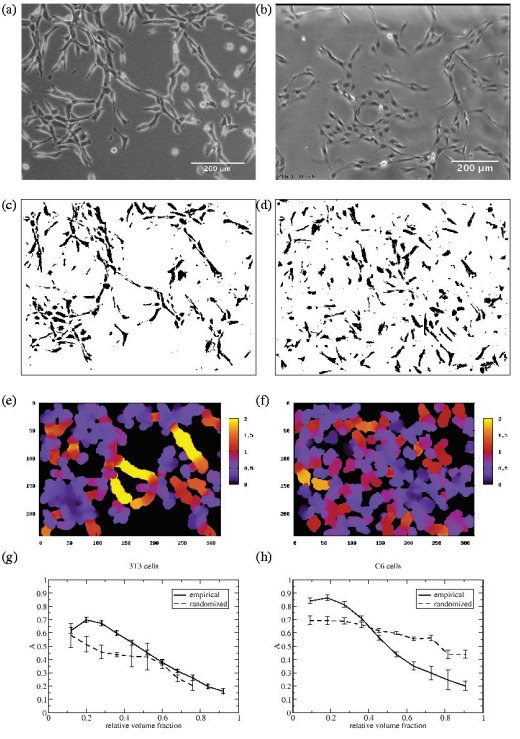

Figure 12: Multicellular linear segments form in in vitro cultures of C6 (a) and 3T3 (b) cells. For morphometric analysis the images were segmented (c), and the resulting clusters randomized without overlaps (d). Maps of local anisotropy (e and f) detect elongated structures as bright yellow areas (e). Although individual cells are elongated, such high values of anisotropy are absent in synthetic images (f), obtained from the randomized image (d). Local cell density strongly influences the anisotropy of both 3T3 (g) and C6 (h) cell configurations. The mean anisotropy value is maximal for culture surfaces with 20% confluence. Error bars of anisotropy values represent the standard error of the mean. [89]

local anisotropy (fig. 12g and h). Local cell density is determined as the surface fraction occupied by segmented cell clusters within a 50 μm wide region: the ratio of the area occupied by the clusters and the selected region. To obtain a measure of confluence, the volume fraction values are normalized by the maximal volume fraction value observed for the particular cell type. At high densities cells fill the substrate and local anisotropy drops. At very low densities cells are separated and no multicellular structures form. At an intermediate density (20% confluence), a maximum in anisotropy values indicates that cells often assemble into linear structures.

Motility is enhanced in elongated structures

Time-lapse microscopic records of C6 cells reveal that the intensity of cell motion strongly correlates with the presence of adjacent, elongated, highly anisotropic structures (fig. 13). As manually tracked cell trajectories demonstrate (fig. 13a), cells intensively move towards and within extending sprouts. After the sprouts became wider, cell motility diminishes again.

For explicit observation of the connection between the local anisotropy and cell motility, the cells were tracked manually and $\mathbf{v}_i(t)$ velocities for various cells i at several time-frames t is calculated. The $A(\mathbf{r}_i(t))$ local anisotropy values at the $\mathbf{r}_i(t)$ position of cells are then coupled to the velocities $\mathbf{v}_i(t)$. As fig. 13b demonstrates, cells tend to be up to three times faster in sprouts than in isotropic cell clusters.

An investigation of branch widening rates reveals that highly anisotropic structures are attractive migration targets. This preference is reflected in fig. 13c as the width of highly elongated and thus anisotropic sprouts increases at a faster rate. As no obvious spatial pattern in cell division rate is observed, the increased sprout widening is resulted by an increased immigration of cells.

In summary, the data in fig. 13 demonstrate that cells preferentially abandon contacts with well-spread cells and move towards adjacent elongated, anisotropic cells, supporting the hypothesis of preferential attachment to elongated cells.

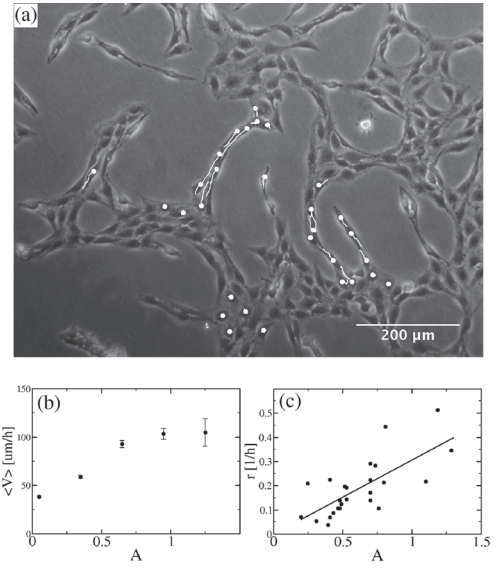

Figure 13: The dynamics of sprout formation in C6 cell cultures on a rigid substrate is visualized by time-lapse microscopy. a: Cell trajectories demonstrate intense motility within elongated structures. Current cell positions are marked with white dots, trajectories covered are drawn with white lines. b: Data obtained from 3000 manually traced positions of more than fifty C6 cells reveal that mean cell velocity is three times greater in highly anisotropic sprouts. Error bars represent the standard error of the mean. c: The manually determined rate of branch widening is also positively correlated with the average anisotropy of the branch. The increased widening reflects increased migration into the branches. [89]

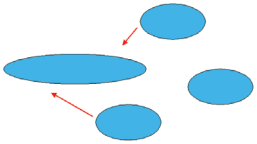

Figure 14: A possible mechanism for network formation is the preferential attachment to elongated cells.

3.2. The preferential attraction model

The analysis of time-lapse recordings of cell cultures led to a possible, new mechanism for network formation: a direct, cell-cell interaction which preferentially guides cells towards adjacent elongated cells (fig. 14). While the molecular basis of such a behavior is unknown, it may involve mechanosensing. Cells are able to respond to variations in extracellular matrix stiffness [34], and an analogous mechanotaxis utilizing cell-cell contacts is also feasible. The cytoskeleton of elongated cells differ from that of round ones, altering the mechanical properties of the cell: preliminary data of recent AFM measurements indicate significant differences in stiffness of round and elongated cells. The analysis of cell culture time-lapse recordings show that close contact with elongated cells indeed enhances and guides cell motility (fig. 13).

To show that such an interaction can indeed generate linear segments and an interconnected network, the hypothesis is implemented in a particle model, where cell shape is deduced from the configuration of surrounding cells. The network formation at different densities is analyzed with this model. Because cell shape is the key feature of cells in the hypothesis, the two dimensional cellular Potts model is also used, where cell shape is explicitly resolved. The balance between multicellular sprouting and surface tension-driven coarsening is analyzed by systematic numerical simulations. In both models, the hypothesis represents an asymmetric, hence out of equilibrium cellular interaction.

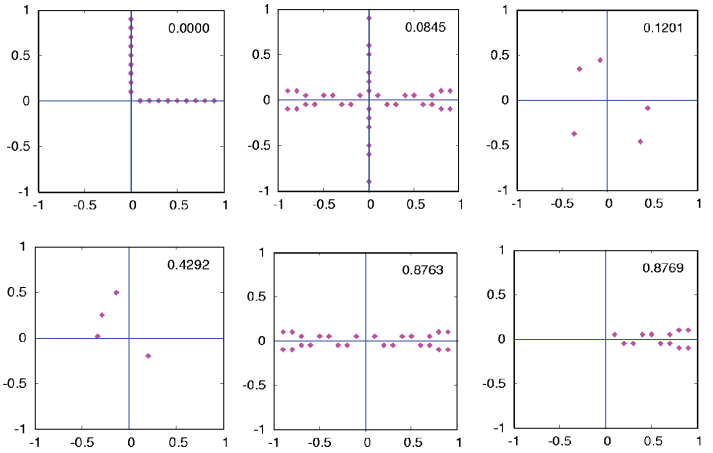

Figure 15: The environmental elongation factor a_j is used to describe the anisotropy of the cell in the particle model. Values in different configurations are demonstrated for a cell in the origin of the plots.

3.3. Interacting particle model

Definition

The hypothesis of preferential attraction towards elongated cells is implemented in a particle model (described in section 1.4.) by defining (i) a measure of cell elongation and (ii) a suitable cell-cell interaction function $\mathbf{f}_{i,j}$ to eq. 1.5. Only local interactions mediated by direct contacts between cells are allowed. As cell shape is not resolved in this model, the contact neighbors are defined as the Voronoi neighbors within a pre-defined range R.

Cell elongation is inferred from the configuration of particles. The anisotropy

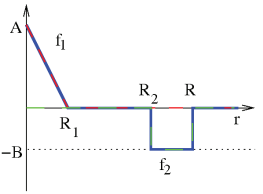

Figure 16: The pair-interaction function describes a soft-core repulsion (f_1) and attraction (f_2) in a limited range $[0 : R]$. The strength of attraction is modulated by the cell elongation of the interacting partner, resulting in a central, but asymmetric attraction.

of particle j, a_j, is constructed as

$$a_j = \frac{1}{n_j} \left| \sum_{d_{kj}<R} \exp\{2i\phi_{kj}\} \right|^2 , \tag{3.1}$$

where n_j is the number of all particles within the interaction radius R around $\mathbf{r}_j$. Vector $\mathbf{r}_k - \mathbf{r}_j$ is at an angle ϕ_{kj} measured from an arbitrarily chosen, fixed reference direction. Therefore, $a_j = 0$ for particles in an isotropic environment and $a_j = 1$ for particles in a highly elongated, linear configuration (fig. 15).

The effect of cellular interactions on cell i is constructed as:

$$\mathbf{f}_i = \sum_j \mathbf{f}_{i,j} = \sum_{j \in V_i} \left\{ [f_1(d_{ij}) + a_j \cdot f_2(d_{ij})] \frac{\mathbf{r}_j - \mathbf{r}_i}{d_{ij}} \right\} \tag{3.2}$$

Here V_i denotes the set of Voronoi neighbors of cell i, $d_{ij} = |\mathbf{r}_j - \mathbf{r}_i|$ is the distance of cells i and j, and a_j is a measure of cell elongation for the interacting partner, cell j. Function $f_1(d)$ is an elastic, soft-core repulsion, ensuring that model cells do not inter-penetrate (fig. 16):

$$f_1(r) = \begin{cases} -A(r - R_1), & \text{for } r < R_1, \\ 0, & \text{for } r \geq R_1 \end{cases} \tag{3.3}$$

where A is a model parameter regulating cell stiffness. Repulsion range R_1 is the size of the organelle-packed region around the cell nucleus. Term $f_2(d)$ contains the cell-cell attraction part of the interaction:

$$f_2(r) = \begin{cases} -B, & \text{for } R_2 \leq r \leq R \\ 0, & \text{elsewhere} \end{cases} \tag{3.4}$$

where B is the parameter regulating the strength of cellular attraction. Since the interaction of cells is local, only cells within a certain $[R_2 : R]$ range will give a non-zero bias. The size of the attraction band around the cell corresponds to the relaxed size of the cell (R_2) and the maximum length of the cell's filopodia (R). The strength of attraction is modulated by the cell shape of the interacting partner, a_j, in eq. 3.2. Since a_j usually varies among cells j, the pair-interactions, unlike Newtonian forces, are asymmetric. By setting $a_j \equiv 1$ for all cells j, a symmetric model is defined, in which the preferential attraction hypothesis is not included.

Simulation results

Simulations were started with randomly scattered cells on a rectangular plane, with periodic boundary conditions. A special initial condition, when cells are packed in the center of the plane, has also been studied.

Based on empirical observations, length scales in the model can be approximated as $R_1 = 10\mu m$ as the core diameter of the cells, $R_2 = 30\mu m$ as the size of a relaxed cell, and $R = 40\mu m$ as the maximum distance of filopodia tip. These values, however, can vary by at least a factor of 2, depending on the cell types and experimental conditions.

Empirically observed cell persistence times ($\tau \approx 0.1 - 5h$) and random movement acceleration magnitudes ($\alpha \approx 50 - 2000\mu m^2/h^3$) measured on single-cell migration assays [85] are used to calibrate a computational time-step to 3 minutes (0.05 h) real time, using the average displacements of cells and eq. 2.6. Model parameter values $\tau = 0.5h$ and $\alpha = 100\mu m^2/h^3$ were used, providing a low diffusion parameter $\mu = 15\mu m^2/h$. Cell stiffness (repulsion) and attraction strengths are set at $A = 160h^{-2}$ and $B = 130\mu m/h^2$. This choice of B represents a strong response to external cues: the ratio of the directed and random velocity compo-

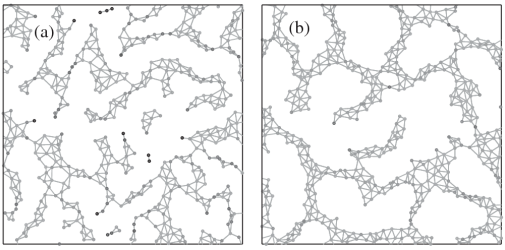

Figure 17: Simulated cells in an $L = 700\mu m$ system with initially randomized positions form linear segments within 30 minutes (a) and connect into a network within 5 hours (b). Connected dots represent cells in contact, the grayscale values of the dots mark the anisotropy of cells. [88]

nents is

$$\frac{B\tau}{\sqrt{2D/\tau}} \approx 10. \tag{3.5}$$

System size L and cell number N were varied for mapping the density-dependence of the model dynamics. Density of cells was measured through surface fraction of overlapping circles with radius R_2 centered on the objects.

At sufficiently high density, randomly scattered cells connect into linear segments within 30 minutes and form networks in several hours (fig. 17). To characterize the pattern size, cells in the configurations were masked with full circles of R_2 diameter size that represents the cell body. The power spectrum of the resulting, filled configurations was calculated as

$$P(q) = \left\langle \left| \sum_j e^{-2\pi i \mathbf{q}\cdot\mathbf{r}_j} \right|^2 \right\rangle \tag{3.6}$$

where each component of $\mathbf{q}$ is an integer multiple of $1/L$. The average $< ... >$ is taken over configurations of different simulation runs.

After the initial connection of the network, the characteristic size of the pattern reaches a quasi-stationary state, where the formation of new connections and the

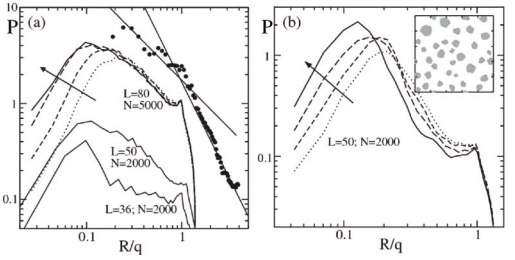

Figure 18: Power spectrum $S(q)$ of cell configurations in the preferential adhesion model (a, curves), in experiments (a, solid symbols) and the symmetric model (b), at various time points and parameter configurations. The dotted, dashed and solid curves were obtained at $t = 25h, 75h, 125h$ and $500h$, respectively. After an initial coarsening, the pattern does not change substantially in the preferential adhesion model, as the forming and disconnecting of branches reaches a balance (a). Two peaks are apparent on the spectra, corresponding to the typical cell size and the characteristic pattern size at $q_*R \approx 10$. Systems with different size or different cell density produce the same characteristic pattern size q_*. At low cell densities ($N = 80$ and $N = 50$) the peak falls off with $1/q$ in good agreement with the data obtained from fig. 11 (solid symbols). The solid lines represent power-law decays with -1 and -2 exponents. In contrast, the symmetric model of uniformly adhering cells (b) continues to coarsen into droplets (inset). [88]

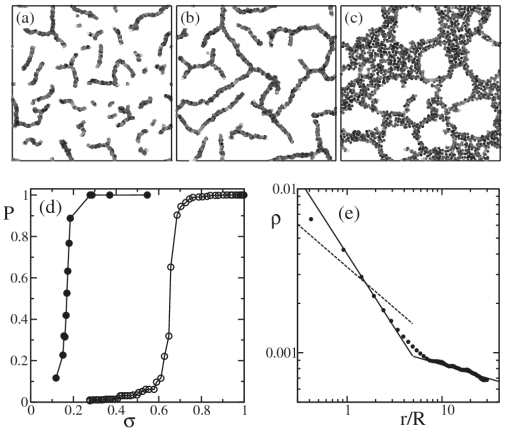

Figure 19: Morphology of the configurations depend on the cell density. Configurations with $N = 2000$ cells are shown in different densities: $N/L^2 = 2 \times 10^4/cm^2$ (a), $3 \times 10^4/cm^2$ (b) and $9 \times 10^4/cm^2$ (c). The relative volume fraction of the largest cluster shows a percolation transition at volume fraction $\sigma \approx 0.2$ (d). The percolation threshold for randomly distributed cells is around 0.67 depicted with the open symbols. The density autocorrelation of the critical cluster (e) exhibits two separate regimes. The solid lines indicate $\rho(r) \sim r^{-0.9}$ and $\rho(r) \sim r^{0.2}$, whereas the dashed line is $\rho(r) \sim r^{-0.5}$ curve. [88]

breaking of the existing branches reaches an equilibrium (fig. 18). The spectrum exhibits two peaks: one corresponding to the characteristic cell-cell distance ($q_c \approx 1/R_2$), the other to the pattern size ($q_* = 1/\ell_*$). This pattern size is approximately the size of ten cell lengths, $\ell_*/R \approx 10$, independent of the system size and only weakly depends on cell density.

Due to the local nature of the interactions, network formation is only possible above a certain density. The density-dependence thus has been studied in a wide range of volume fractions (fig. 19). Connectivity is described by calculating the relative surface fraction of the largest cluster (P) as a function of total surface fraction, σ. The percolation threshold is at volume fraction $\sigma \approx 0.2$, a relatively

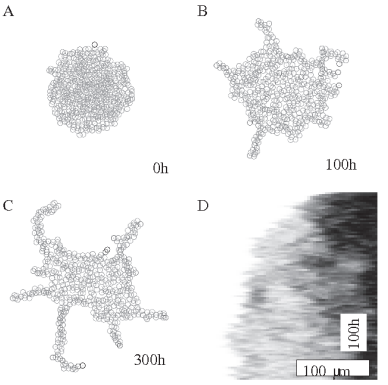

Figure 20: Simulation runs initiated from a cell aggregate, the stationary state of the symmetric adhesion model, grow branches. Panels A-C show cell configurations throughout the simulation. A kymogram of a representative sprout (D) depicts a sprout extending throughout the simulation: the top of the image shows the cell density profile along the sprout axis at $t = 0$, and at the end of the simulation in the bottom of the image. The profile shown demonstrates that sprouts grow with decreasing speeds, as the process is driven by random noise. [10]

low value compared to the 0.67 obtained with randomly positioned cells (fig. 19d).

To compare the pattern with the chemotactic model of Gamba et al. [29], the mean density ρ of the critical cluster has been calculated as the function of radius (r). For radii larger than the cell size ($1 < r/R < r_c$), the density is described as $\rho(r) \sim r^{-0.9}$ and above a crossover length, $r_c/R \approx 6$, $\rho(r) \sim r^{-0.17}$ (fig. 19e). This is in good agreement with the slope of the power spectra decreasing with $P(q) \sim q^{-1}$ (fig. 18), both in simulation and model configurations. The chemotactic model of Gamba et al. [29], however, produces patterns with fractal-like $\rho(r) \sim r^{-0.5}$, illustrated on fig 19e as a dashed line.

Simulations started from a dense cluster develop sprouts spontaneously (fig. 20). The sprouts, however, do not describe biological sprouting: the growth profile of the sprouts shows decreasing growth speeds (fig. 20d) compared to the steady sprouting observed experimentally (see fig. 37). Also, the forming branches tend

to move sideways due to the lack of adhesion or friction in the model. This reflects the lack of active persistent locomotion.

3.4. Preferential adhesion in the cellular Potts model

Definition

Using the CPM defined by Graner and Glazier [33], the preferential attachment to elongated cells is implemented by introducing a suitably altered probability function w into eq. 1.8 and a measure of cell elongation.

Cell shape is resolved in the model, therefore an explicit definition of elongation is possible. The measure of anisotropy for cell i is denoted by θ_i, and is obtained from the inertia tensor of the Potts domain representing the cell as

$$\theta_i = \sqrt{\frac{\lambda_1}{\lambda_2}} - 1, \tag{3.7}$$

where $\lambda_1 \geq \lambda_2$ are the two eigenvalues of the inertia tensor.

The probability of copying the spin value $\sigma(\mathbf{a})$ at lattice site $\mathbf{a}$ to an adjacent lattice site $\mathbf{b}$ is given by 1.8. The motion bias $w(\mathbf{a} \rightarrow \mathbf{b})$ is used to represent a tendency to contact elongated cells as

$$w(\mathbf{a} \rightarrow \mathbf{b}) = \gamma \left[\chi(\mathbf{a}) - \chi(\mathbf{b})\right] \cdot \sum_{\mathbf{c}} \theta_{\sigma(\mathbf{c})} \tag{3.8}$$

where parameter γ sets the strength of the bias relative to the other, surface tension and volume constraint terms in eq. 1.8 and function $\chi(\mathbf{r}) = 1$ for sites $\mathbf{r}$ belonging to a cell, and zero otherwise (see eq. 1.9). The summation in eq. 3.8 goes over only those neighbor sites of $\mathbf{b}$ that belong to cells other than $\sigma(\mathbf{a})$ or $\sigma(\mathbf{b})$: $\sigma(\mathbf{c}) \notin \{0, \sigma(\mathbf{a}), \sigma(\mathbf{b})\}$.

The $\chi(\mathbf{a}) - \chi(\mathbf{b})$ expression ensures that only cells (and not the medium) exhibit the preference. For $\sigma(\mathbf{a}) = 0$ and $\sigma(\mathbf{b}) > 0$, the elementary step considered is a cell retraction, while for $\sigma(\mathbf{a}) > 0$ and $\sigma(\mathbf{b}) = 0$, the step represents cell expansion. These steps may involve loosing or gaining contact with a certain cell $\sigma(\mathbf{c})$ at an adjacent lattice site $\mathbf{c}$. Furthermore the expression also assumes that the amount of attraction depends only on the contact target: if site $\mathbf{b}$ is occupied

by a cell ($\chi(\mathbf{b}) = 1$) then no other cell ($\chi(\mathbf{a}) = 1$) has any advantage to occupy that adhesion site. For example, if cell $\sigma(\mathbf{a})$ attempts to move next to cell $\sigma(\mathbf{c})$, and the separating site is empty ($\sigma(\mathbf{b}) = 0$) and no other cell is near to site $\mathbf{b}$, then $w = \gamma\chi(\mathbf{a})\theta_{\sigma(\mathbf{c})}$. Therefore, the probability $p(\mathbf{a} \to \mathbf{b})$ is increased if $\theta_{\sigma(\mathbf{c})}$ is high.

The $w(\mathbf{a} \to \mathbf{b})$ term can also be considered as an asymmetric extension of the J_{ij} adhesive interaction. This is more obvious if $w(\mathbf{a} \to \mathbf{b})$ is written in the form of

$$w(\mathbf{a} \to \mathbf{b}) = -\gamma \sum_{\mathbf{c}} [J_{\mathbf{a}\to\mathbf{b}}(\sigma(\mathbf{a}), \sigma(\mathbf{c})) - J_{\mathbf{a}\to\mathbf{b}}(\sigma(\mathbf{b}), \sigma(\mathbf{c}))] \tag{3.9}$$

where

$$J_{\mathbf{a}\to\mathbf{b}}(i,j) = \begin{cases} 0 & \text{if } i = j,\ i = 0,\ j = 0,\ j = \sigma(\mathbf{a}) \text{ or } j = \sigma(\mathbf{b}); \\ \theta_j & \text{otherwise.} \end{cases} \tag{3.10}$$

In general, $\theta_i \neq \theta_j$, therefore $J_{\mathbf{a}\to\mathbf{b}}(i,j)$ is an asymmetric matrix. The asymmetry is instrumental in transforming the model into a stochastic system where configuration and transition probabilities do not satisfy detailed balance. As the example in fig. 21 demonstrates, configuration (d) can be reached by at least two different sequences of steps from configuration (a). Due to symmetry, the $\wp$ transition probabilities between states (a) and (b) are the same as those between (a) and (c). However, if cell A is more attractive than cell B, then the (b) $\to$(d) transition is more frequent than the (c) $\to$(d) transition. Furthermore, the (d) $\to$(b) transition is less frequent than the (d) $\to$(c) transition:

$$\frac{\wp[(b) \to (d)]}{\wp[(c) \to (d)]} > 1 > \frac{\wp[(d) \to (b)]}{\wp[(d) \to (c)]} \tag{3.11}$$

If the equilibrium probability of states (b), (c) and (d) are P, P and Q, respectively, then the detailed balance condition requires $P\wp[(b) \to (d)] = Q\wp[(d) \to (b)]$ and $P\wp[(c) \to (d)] = Q\wp[(d) \to (c)]$. However, the resulting

$$\frac{\wp[(b) \to (d)]}{\wp[(c) \to (d)]} = \frac{\wp[(d) \to (b)]}{\wp((d) \to (c)]} \tag{3.12}$$

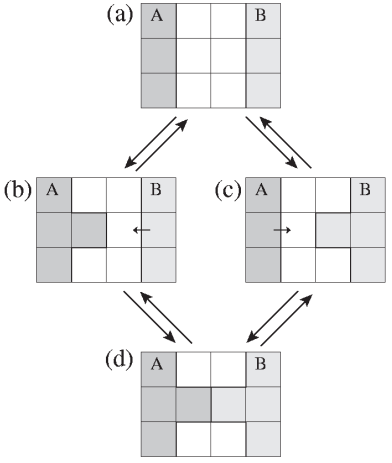

Figure 21: Demonstration of how the asymmetric nature of the interaction results in a driven, out of equilibrium system. By symmetry arguments the first step has the same probability in both paths: $\wp$[(a) $\rightarrow$(b)] = $\wp$[(a) $\rightarrow$(c)] and $\wp$[(b) $\rightarrow$(a)] = $\wp$[(c) $\rightarrow$(a)]. However, if cell A is more attractive than cell B ($\theta_A > \theta_B$), then the (b) $\rightarrow$(d) transition is more frequent than the (c) $\rightarrow$(d) transition (the elementary steps indicated by arrows in (b) and (c), respectively). Furthermore, the (d) $\rightarrow$ (b) transition is less frequent than the (d) $\rightarrow$(c) transition. As a result, the steady-state probabilities of the four configurations will not satisfy detailed balance. [89]

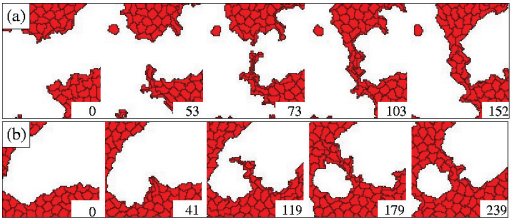

Figure 22: Formation of new branches in the stationary state of the model. Fluctuations initiate sprouts, and the resulting elongated structure attracts further cells. If the expanding branch connects to another cluster it becomes stable, otherwise it degenerates, hence the sprout length is limited. Time shown on the images is indicated in MCS. [89]

condition contradicts eq. 3.11. Therefore, in the asymmetric model the transition probabilities cannot satisfy the detailed balance condition, and thus the dynamics cannot be interpreted as relaxation of an energy functional to thermal equilibrium.

Simulation results

The model was studied by simulations in a square area of size $L \times L$ with closed boundary conditions. The initial configuration consisted of N randomly positioned cells and an arbitrary domain representing the cell-free areas on the substrate. The preferred cell size is set to 50 lattice sites, adjusting the distance of two lattice points to approximately $\sim 1\mu$m. Based on the mean square displacement versus time curves of non-interacting cells (see eq. 2.6 and [85]), one Monte-Carlo time step (MCS) corresponds to ~ 2 minutes in real time.

For a set of parameter values, the model exhibits sprouting behavior, reminiscent of those observed in experiments (fig. 22). After the initial bud appears, the leading – elongated – cell attracts other cells from the pool at the base of the sprout. Cells within the sprout continue to migrate until they connect to another cluster of cells. At that point the branch is established and becomes stable. Due to the effective surface tension present in the system [24], branches can also break up, and this way coarsen the pattern.

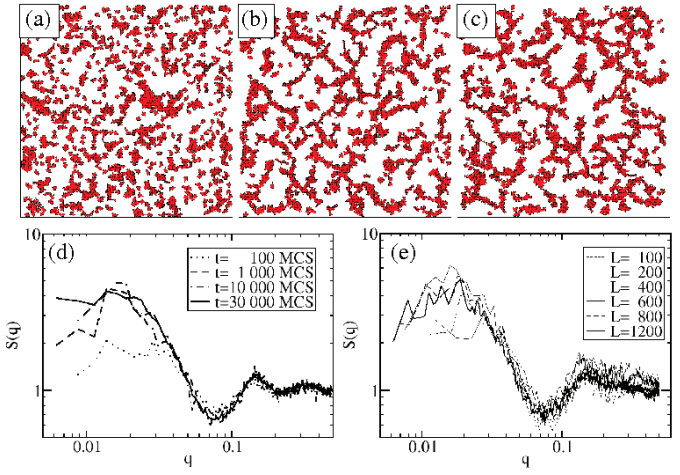

Figure 23: The model reaches a stationary state where surface tension-driven coarsening is balanced by the formation of new sprouts. Configurations in the model are shown at t=100 (a), 1000 (b) and 30,000 (c) MCS. Structure factors averaged over 10 independent runs show that the emerged pattern does not change its statistical characteristics after 1000 MCS (d). However, the resulting pattern is not frozen: branches still form and break up, as visualized in fig. 22. The characteristic pattern size $\ell_* \approx 80\mu$m is independent of the system size L in the $L \gg \ell_*$ limit as the structure factors of configurations obtained from systems with increasing sizes indicate (e). [89]

If parameter values are favorable for sprouting in the system, then after an initial transient regime the balance of surface tension driven coarsening and the growth of new branches result in a quasi-stationary state (fig. 23). After the first 1000 MC time-steps the statistical properties of the network-like pattern does not change substantially, indicated by the ensemble-averaged structure factors $S(q)$ (fig. 23d). The characteristic pattern size $\ell_* \approx 80\mu$m is determined by the dynamics, and does not depend on the system size for $L \gg \ell_*$ (fig. 23e).

The effects of the symmetric and asymmetric adhesion terms in eq. 1.8 were studied systematically with simulations. Parameter γ, characterizing the preference of elongated cells, is responsible for sprouting activity in the model (fig. 24a). As cell-cell contacts increase the CPM energy u by α, an effective attraction requires $\gamma > \alpha$. For a fixed value of γ, the two independent parameters α and β control the effective surface tension, and thus the characteristic pattern size (fig. 24b). Cell shape is determined by the relative balance of surface tension and anisotropic bias: if the anisotropic bias dominates, individual cells tend to become extremely elongated.

For a fixed value of model parameters, cell density determines the connectedness of the structure, and it also influences the characteristic pattern size (fig. 25a). Cell density is measured as a volume fraction, i.e., the ratio of the area covered by cells and the overall system size. At densities higher than 0.55, the linear structures gradually disappear. At densities under 0.20, there are not enough cells to connect into clusters. As in the case of the particle model, within an intermediate range of densities, the characteristic pattern size ℓ depends only weakly on the density (fig. 25b).

The local anisotropy of the configuration was calculated as the function of the local volume fraction for a range of cell densities (fig. 25c). At low densities the anisotropy tends to be higher, and it exhibits a maximum at a density ≈ 0.4. The peaked curve is thus qualitatively similar to the empirical data presented on fig. 12g, h. The lower values of anisotropy reflect the fact that branches in the model are usually more than a single cell wide.

The energy expression, eq. 1.8, contains elastic-like terms involving δA_i, the deviation of the i-th cell's area from its target value. Thus, δA can be interpreted as a measure of hydrostatic pressure. In the contact inhibition model of chemotaxis

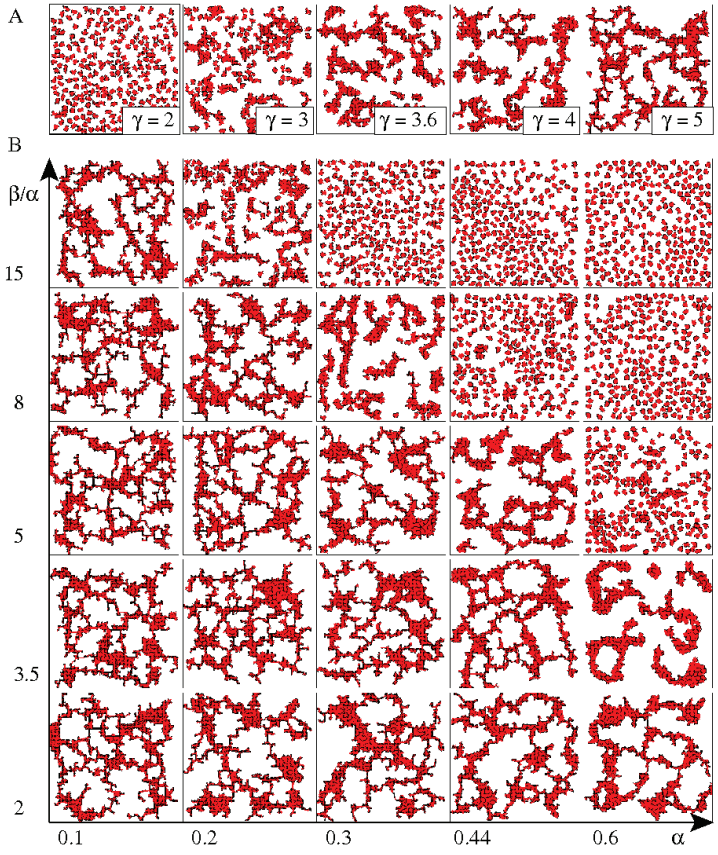

Figure 24: Morphology diagram of the stationary state as a function of γ, the strength of attraction to elongated cells, and parameters α and β specifying an effective surface tension in the model. A: For large enough γ a connected pattern arises. Typical configurations are shown for $\alpha = 0.3$ and $\beta = 2.4$. B: For a fixed $\gamma = 3.6$, increasing α results in coarser structures, while increasing β yields individual cells. $L = 200$, $N = 250$. [89]

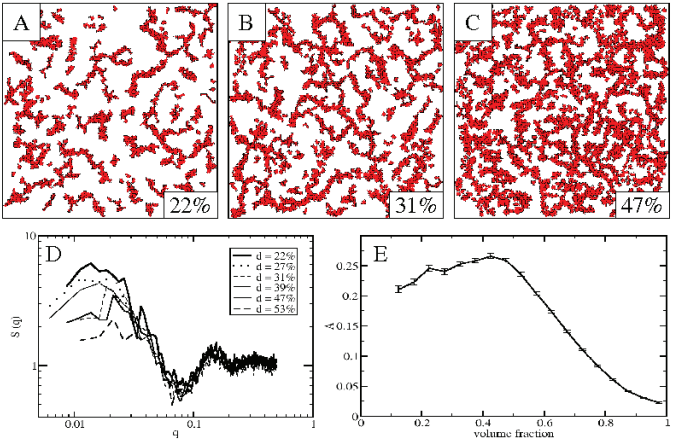

Figure 25: The stationary pattern depends on the cell density. Typical model configurations are shown for volume fractions of 0.22 (a), 0.31 (b) and 0.47 (c). The normalized structure factors (d) reveal a peak at $\ell_* \approx 80\mu$m for densities between 0.30 and 0.50. The local anisotropy of the configuration as the function of the local volume fraction (e) reveals a maximum at a density ≈ 0.4. The peaked curve is thus qualitatively similar to the empirical data presented in figs. 12g and h. $\alpha = 0.3$, $\beta = 2.4$, $\gamma = 3.6$, $L = 400$. [89]

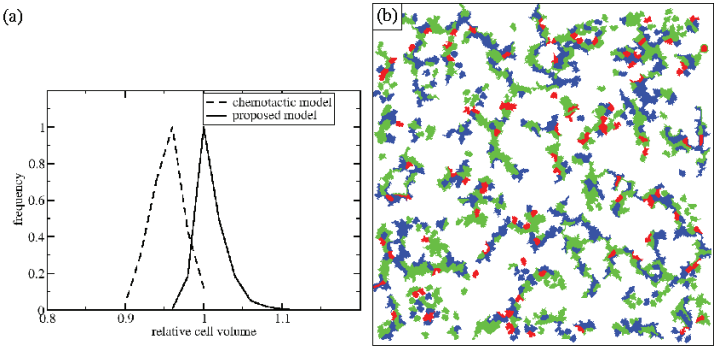

Figure 26: In the proposed model, the patterning mechanism differs from the chemotactic model of Merks et al. [58]. a: The size distribution of the simulated cells reveals that in our model the cells are not compressed, but are rather expanded. b: The location of stretched (blue) and compressed (red) cells show no obvious regularity within a typical configuration. Cells with the target area are shown in green. [89]

of Merks et al. [58], branching occurs due to an instability which involves the internal, hydrostatic-like pressure within the aggregates and a radially weakening effective surface tension. To compare the present patterning mechanism to that of Merks et al. [58], we characterized cell compressions in both models. The distributions of δA are shown in fig. 26a. As expected, cells in the Merks model are under compression. In contrast, cell areas in our model fluctuate around the target size, with slightly more expanded cells then compressed cells. Fig. 26b shows the distribution of compressed (red) and expanded (blue) cells in a typical configuration generated by our model. The random mixture of compressed and expanded cells also indicate that hydrostatic pressure cannot play a substantial role within our model. Thus, the two models generate branching structures by clearly different mechanisms.

3.5. Discussion

Attraction to elongated cells

Statistical evidence is provided that various cell types such as C6 gliomas, C2C12 myoblasts or 3T3 fibroblasts form multicellular linear arrays in a certain range of cell densities. This patterning cannot be explained by the usual models of random motility and isotropic cell-cell adhesion which predicts gradually growing droplets [7], furthermore, the previously proposed models of vasculogenesis do not apply in these experimental settings.

Analysis of time-lapse recordings reveals a remarkable change in motility when cells become incorporated into multicellular sprouts, and that these sprouts are attractive migration targets: due to cell migration, the population of sprouts increases substantially faster than the population of isotropic cell groups. As highly elongated cells initiate and guide the motility of adjacent cells, we argue that the generic ability to form cellular networks can be attributed to this preferential attraction to elongated cells.

The cell biological basis for such a preference is not yet known. Cells in elongated structures are possibly under mechanical tension, therefore the micromechanical properties of their cytoskeleton are altered [46]. Cells are able to detect mechanical differences in their surroundings, as has been shown with the

variations in extracellular matrix stiffness [50, 34, 44]. A similar mechanosensing is feasible between cells: for example, VE-cadherin, a major cell-cell adhesion receptor of vascular endothelial cells, was recently shown to be incorporated in cell surface mechano-sensing complexes [95].

Numerical modeling

Each modeling attempt includes simplifications and necessarily omits certain properties of the real system to be modeled. Different frameworks, however have different approaches and may complement each other if used for the same description. Therefore, it is intrinsically valuable to cast the biologically relevant hypothesis into very different modeling frameworks, and show that the emergent multicellular behavior is independent of the choice of framework.

The preferential attraction to elongated cells was studied with an interacting particle model based on the OU process described in section 1.4. In the model, networks form from initially scattered cells, in a wide range of cell-densities above relative surface fraction 0.2. The emerging patterns reach a quasi-stationary state, in contrast with the coarsening networks produced in the chemotactic model of Gamba et al. [29].

The hypothesis of preferential attraction between cells is implemented in the form of a special attraction, where the strength of attraction depends on the anisotropy of the interacting partner. The implementation of the interaction term is very direct, the anisotropy of cells, however, is derived indirectly, as cell shape is not resolved in the model. We assume, that the shape of the cells is defined by the surrounding cell configurations.

The preferential attachment hypothesis was also tested in the cellular Potts model, where cell shape is explicitly represented and a more direct measure of cell elongation is possible. Factors determining motility, however are hidden in the stochastic simulation rules and, therefore, are less transparent. Nevertheless, interactions in the model are truly local in the sense that only adjacent cells interact. Due to the wide use of the Potts formalism, comparison between models built upon the same framework are more feasible, as in fig. 26.

To account for the preferential attraction of elongated cells, the CPM is aug-

mented with transition probabilities that depend on the actual state of interaction partners. This asymmetric attraction term in the transition probabilities results in an inherently non-equilibrium system, thus is fundamentally different from the anisotropic interaction suggested by Zajac et al. [107], where the dynamics (apart from the continuity constraints) can be still derived as a relaxation of an energy functional of the spin configurations. However, it is not clear why such a global target/cost function should always exist to describe the behavior of multicellular systems – non-equilibrium transition rules may be useful to model other systems as well.

In the Potts formulation, cell-cell adhesion is described as an effective surface tension, which drives the system to minimize open surfaces (cell surfaces unattached to adjacent cells), hence it works to destroy sprouts. When a branch connecting two clusters is about to break, it will consist of elongated (and strained) cells which connect the clusters and adhere to both. According to our preferential attachment hypothesis, such a cell is an attractive migration target and the resulting active inflow of cells into the strained area will offset the coarsening tendency of surface tension. Pattern size depends slightly more on cell density, compared to the particle model, which could be the result of the complete absence of motion persistence of the Potts cells.

Mechanism of sprout formation

Network formation through sprouting occurs in a markedly different way from the gradual coarsening of an initially uniform density field and its possible arrest, characteristic for colloid gels (see, for example Foffi et al. [21]) or for several models proposed for vasculogenesis. In particular, in the chemotactic model [29] and in the mechanical model [54, 65] the emerging pattern is static, the rearrangement of the created network is only possible by further gradual coarsening.

In our model, the elongation of the invading cell catalyzes the recruitment of further cells to into the sprout. Cell-cell adhesion alone would keep cells at the sprout base where they are well surrounded with neighbor cells. The model of Merks et al. [58], however, also produces sprouts with biologically plausible assumptions, therefore a more direct comparison is performed. The two mod-

els were shown to result in different states of cell areas, a potential way to test their validity. The most striking difference is that the chemotaxis-based model is pressure-driven, and cells are predicted to be compressed in the aggregates. Patterning occurs due to an instability which involves the internal, hydrostatic-like pressure within the aggregates and a radially weakening effective surface tension. Therefore, aggregate surfaces are unstable and sprouting is driven by an internal pressure gradient. In contrast, in our model, cells are typically not compressed, which prevents the build-up of pressure gradients within the aggregates. We argue, that our approach fits better the in vitro cell cultures with low cell densities - where cells are well-spread or moderately stretched - based on the observed reduction in cell area after severing cell attachments to the substrate, e.g., by trypsin treatment.

The inherent asymmetry of the preferential attraction hypothesis might be an important feature that separates it from other models that evolve with a gradually coarsening pattern. The difference is demonstrated in the particle model by starting a simulation from the stationary state of the symmetric model, a dense cell aggregate. The asymmetry dilutes the aggregate by sprouting (fig. 20). In the CPM, spontaneous sprouting is observed during patterning (fig. 22).

Although sprouting occurs in the models, the dynamics is not realistic: the short persistence of cells and the lack of self-propulsion produces branch growth with decreasing speeds, resulting in too short sprouts. Experimentally observed sprouts, however, have a linear growth profile and can extend to the length of tens of cells (see fig. 37).

4. Cell streaming in monolayer cultures

Collective motion of cells is instrumental in development and in certain pathophysiologies, where a number of cells and tissue are transported and deformed as a result of the cooperation of multitude of cells [60]. Such processes include not only the de novo vascular network formation, but gastrulation, wound healing or the revascularization of damaged tissue by existing vessels. The behavior and mechanisms of these cellular cooperations, however, are poorly understood.

Probably the best studied collective cell motion is cell sorting, where a mixture of various type cells segregate from a disorganized starting configuration [76, 97]. The process is explained with the differential adhesion hypothesis (DAH) [84]: different cell types have different adhesion properties that, according to the DAH, eventually results in the spatial segregation of the different cell types. Implementations of the DAH using the CPM [32] or lattice free variants [66] successfully reconstruct the experimental behavior as well as the time course of the process. Suitable extensions of these models can describe cell intercalation during gastrulation [107], chemotaxis-driven cell movements during vascular assembly [58, 57, 2], or tumor growth [16]. However, the motion of cells during sorting is diffusive within the bulk environments [76], although some temporal and spatial correlations are detectable [97].

Motion of polarized cells, which maintain their migratory direction in time, in high density cell cultures is less understood. Most studies addressing this problem have investigated the expansion of epithelial cell sheets or other monolayers into an empty area or 'wound'. During the expansion, cells at the monolayer boundary [17] or within a broader layer [92] exert substantial traction forces and are thought to pull the passive bulk of the sheet forward [76, 13].

Recent studies on the motion of kidney epithelial (MDCK, [37]) or endothelial (HUVEC, [101]) cells within monolayers, as well as immune cells in explanted lymph nodes [5] have indicated an intriguing motion pattern. These cells exhibit an apparently undirected, yet correlated, streaming behavior even in the absence of directed expansion of the whole monolayer. This type of motion is clearly different from both the uncorrelated diffusive activity of cell sorting experiments as well as from the external chemotactic gradient-driven motility.

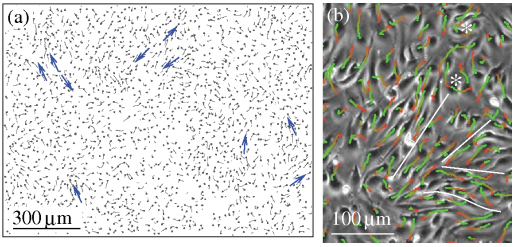

Figure 27: Cell movement within a BAEC monolayer is visualized through cell trajectories. (a): A velocity field snapshot is indicated by short trajectories, obtained during 30 minutes. Cell centers are marked with black dots. Blue arrows show groups of cells moving together in streams. (b): A phase-contrast image detail with superimposed cell trajectories depicting movements during one hour. Red-to-green colors indicate progressively later trajectory segments. Adjacent BAEC streams moving in opposite directions are separated by white lines, vortices are denoted by asterisks. [87]

In this chapter the statistical properties of the collective streaming motion within endothelial cell monolayers is described and modeled.

4.1. Empirical findings

Movement patterns within endothelial cell monolayers were observed in cultures of three different kinds of endothelial cells – bovine capillary (BCE), bovine aortic (BAEC) and human umbilical cord vein (HUVEC) – on Matrigel- or fibronectin-coated tissue culture plastic (see table 1 for details). Confluent cultures, under conditions favorable for cell motility were recorded for 24 hours using an automatized optical microscopy apparatus as described in section 2.1.. A representative set of the resulting image sequences were analyzed by an automatic cell tracking procedure (see section 2.3.). As trajectories in fig. 27 demonstrate, endothelial cells form streams in monolayers: 5-20 cells move together in narrow, chain-like groups. The monolayers contain vortices, and adjacent streams move in opposite directions. The resulting shear lines separate cells with substantial velocity differences.

Cell type	Substrate	Cell density [1000/cm^2]	S [μm/h]	τ [min]	$\mathbf{V}(\mathbf{r})$ sample size [cells]
BAEC	Matrigel	80	33 ± 2	33 ± 3	1100
BCE	Matrigel	40	13 ± 3	40 ± 10	500
HUVEC	Matrigel	40	14 ± 2	112 ± 48	600
HUVEC	Matrigel	20	14 ± 2	110 ± 50	500
HUVEC	Fibronectin	70	14 ± 2	220 ± 170	1000
HUVEC	T.C. plate	40	18.3 ± 0.3	49 ± 7	N.A.

Table 1: Cell types observed and analyzed in cultures on different substrates. Cells were plated in high density, except for one control experiment. Trajectories of cells were analyzed through displacement versus time function and motility parameters (S: cell speed, τ: persistence time) were fitted, using Fürth's formula (eq. 2.6). The last column displays the number of cells used to construct the flow-fields $\mathbf{V}(\mathbf{r})$.

To better understand this collective cell flow characteristic for endothelial monolayers, below we calculate widely used and new statistical measures of individual and group cell motion. These measures facilitate the comparison of various experimental systems exhibiting streaming behavior, and are also needed to test computational models aiming to explain the phenomenon.

Cell movement statistics

The motion of individual cells is evaluated in terms of average cell displacement [19, 52], D, over a time period t as

$$D(t) = \sqrt{\langle (\mathbf{r}_i(t+t_0) - \mathbf{r}_i(t_0))^2 \rangle_i} \tag{4.1}$$

where $\mathbf{r}_i(t)$ denotes the center of cell i at time t, $\langle ... \rangle_i$ is an average over all possible cells, and t_0 is an arbitrary reference frame of the image sequence analyzed. The empirical $D(t)$ curves indicate a persistent random walk behavior in endothelial monolayer cultures, as the average displacements are well fitted by eq. 2.6. The fitted parameter values, summarized in table 1, scatter considerably: by a factor of two (S) and five (τ) depending on the cell line and substrate combination used.

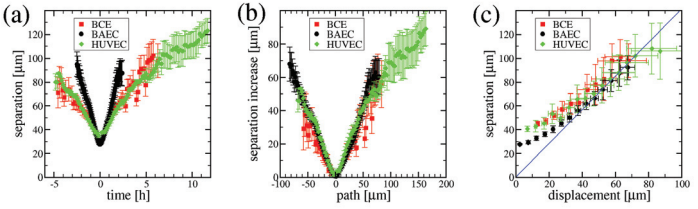

Figure 28: Cell separation within the monolayers. (a): Average separation, $D_2(t)$, of cells adjacent at an initial time $t_0 = 0$. (b): Increase in separation from the average cell size value $D_2(t_0)$ versus the path length (time scaled by mean velocity S). (c): Separation, $D_2(t)$, versus the average displacement of cells, $D(t)$. The blue line of slope $\sqrt{2}$ indicates an uncorrelated movement of cell pairs as derived in eq. 4.4 Error bars indicate SEM. [87]

Another, longer-term property of collective flow is its ability to maintain adjacency of cells. The amount of mixing within the monolayer is indicated by how quickly initially adjacent cells separate from each other. Thus, the average distance between cell pairs that are adjacent in a reference time point t_0 is calculated for each time t as

$$D_2(t) = \sqrt{\langle (\mathbf{r}_i(t) - \mathbf{r}_j(t))^2 \rangle_{(i,j)\in Q}} \tag{4.2}$$

where $\langle ... \rangle$ denotes average over all cell pairs i and j that are neighbors at the reference time t_0 (the set Q).

As the average distances of 100 independent cell pairs reveal (fig. 28a), cells approach and separate in a symmetric process, and the duration of their adhesion (if any) is not resolved well in our analysis. The differences seen in fig. 28a originate primarily from differences in cell speeds: when neighbor separation is plotted against the path length (time scaled by average velocity S), the three data sets collapse around the origin (fig. 28b).

Changes in cell-cell distance (D_2) is compared to the mean cell displacements (D) in fig. 28c. When the separation is large compared to the initial distance of

the cell pair, eq. 4.2 can be approximated as

$$\begin{aligned} D_2^2(t) &\approx \left\langle \left[(\mathbf{r}_i(t) - \mathbf{r}_i(t_0)) - (\mathbf{r}_j(t) - \mathbf{r}_j(t_0)) \right]^2 \right\rangle \\ &= 2D^2(t) - 2\left\langle (\mathbf{r}_i(t) - \mathbf{r}_i(t_0))(\mathbf{r}_j(t) - \mathbf{r}_j(t_0)) \right\rangle \end{aligned} \tag{4.3}$$

where the averages are calculated over the cell pairs $(i, j) \in Q$. For independent cell movements the last term in eq. 4.3 vanishes, leaving

$$D_2(t) \approx \sqrt{2} D(t) \tag{4.4}$$

Therefore, in fig. 28c the asymptotic linear relation between average cell displacement and neighbor separation with a slope of $\sqrt{2}$ indicates a substantial mixing and an uncorrelated long-term behavior within the monolayer.

Average flow fields

As cells of a monolayer constrain the possible movements in their vicinity, correlation is expected in the motion of adjacent cells. In particular, immediately in front of a moving cell, movement in the opposite direction (i.e., towards the cell) is unsustainable and therefore expected to be rare. Unfortunately, there are no established statistical descriptions of streaming cell motility. The co-moving domains are local and randomly oriented within the whole cell culture, therefore, the large-scale rotational symmetry of the system is retained and spatial autocorrelation functions (see, for instance eq. 3 of Haga et al. [37]) depend only on the magnitude and not on the direction of their argument. Thus, such functions are not capable of describing the width and length of streams.

The average flow field around moving cells, $\mathbf{V}(\mathbf{r})$, is a measure sensitive to the local cell movement pattern. For a given cellular velocity field this procedure assigns reference systems co-aligned with the movement of each cell, and averages the velocity vectors observed at similar locations $\mathbf{r}$. The vectors of $\mathbf{V}(\mathbf{r})$ diminish in a hypothetical ensemble of statistically independent cells, as they are averages of independent random vectors.

To calculate $\mathbf{V}(\mathbf{r})$, for each cell i at time t the whole configuration is rotated

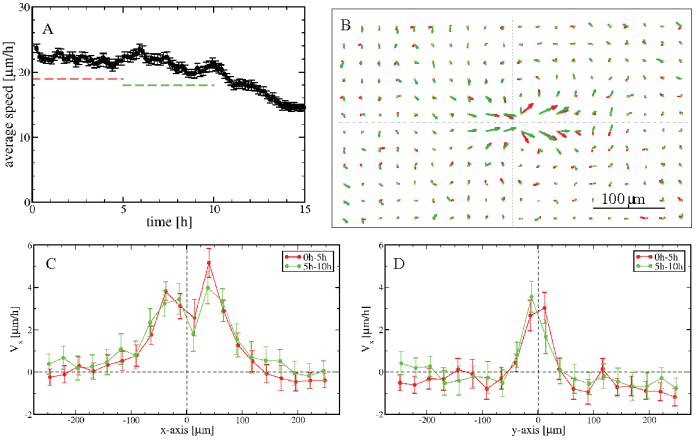

Figure 29: Stability of flow field calculations, in a high cell density HUVEC culture. (a): Average cell velocities during the recording (error bars indicate the standard error of the mean). (b): Flow fields $\mathbf{V}(\mathbf{r})$, calculated from the first and second five hours, are depicted in red and green, respectively. The parallel component of $\mathbf{V}(\mathbf{r})$ along the parallel (c) and orthogonal (d) axes indicate the similarity between the two flow fields. [87]

around $\mathbf{r}_i$ so that $\mathbf{v}_i$, the velocity of cell i, is aligned to a reference direction $\varphi = 0$ (fig. 10). The rotated displacement vectors are then binned according to a two-dimensional lattice B. The procedure is repeated for every cell i and multiple time points, and the bins are averaged resulting in a population- and time-averaged displacement field $\mathbf{V}(\mathbf{r})$. The procedure is further detailed in the section 2.3.

The averages were calculated from at least 30 independent data values per grid point, and the estimated SEM values are represented by a color code. The robustness of this statistical measure is demonstrated by comparing the flow fields of two consecutive time segments of culture recordings exhibiting similar behavior (fig 29).

Fig. 30 shows representative flow fields obtained from cultures with various

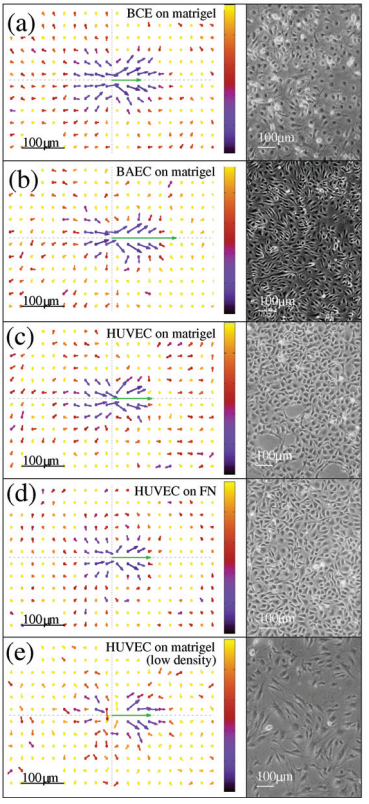

Figure 30: Monolayers of various endothelial cells exhibit similar flow fields on both Matrigel and fibronectin substrates. The local spatial correlation of cell movements were characterized by $\mathbf{V}(\mathbf{r})$, the average flow field that surrounds moving cells. Arrows indicate velocities as one hour displacements, the green arrow in the origin represents the average velocity of cells. For better visibility, vector lengths are scaled by a factor of five. Cultures with sufficient density (a-d) show streaming behavior, indicated by the similarity of average velocity vectors obtained in front of and behind the moving cells. The co-movement drops rapidly in the lateral direction, an indication of the local asymmetry of the streams. In a subconfluent culture (e) the correlation structure is less pronounced. The color code indicates the estimated relative SEM of the vectors: black corresponds to zero, yellow indicates 1. A corresponding phase-contrast image of the cultures are shown on the right. [87]

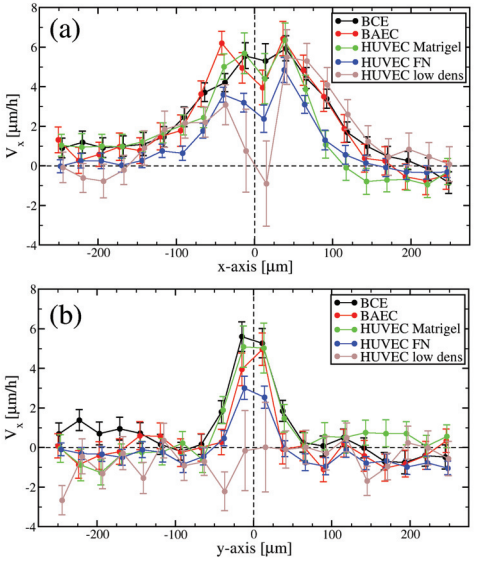

Figure 31: Empirical flow field profiles along two orthogonal axes. For better comparison of data presented in fig. 30, the parallel (V_x) component of the average velocity vectors along the axes parallel (x, panel a) and perpendicular (y, panel b) to the direction of motion are plotted. To reduce symbol overlap, individual data sets are slightly shifted horizontally. [87]

cell-ECM combinations and cell densities (see table 1 for culture parameters). Thus, fig. 30 includes data from both high density monolayer cultures (panels a-d) and a subconfluent, lower density culture as a comparison (panel e). For a better comparison of the flow fields, in fig. 31 we present the parallel component of $\mathbf{V}(\mathbf{r})$ along two orthogonal lines, one parallel (x axis) and one perpendicular (y axis) to the direction of motion.

Flow fields derived from monolayer cultures reveal the presence of velocity correlations exceeding a spatial range of 200 μm, much larger than the typical cell diameter – the mean distance between adjacent cell centers – of 30-40 μm (see fig. 28). Streaming behavior is indicated by the similarity of average velocity vectors obtained within an elongated area surrounding the origin. In the lateral direction, the average velocity drops quickly and in some cases reverses direction (fig. 31) – an indication that streams are narrow and adjacent streams move in opposite directions. Remarkably, very similar correlation structures are seen in all three types of endothelial cell monolayer cultures investigated, irrespective of the underlying extracellular matrix substratum used. In subconfluent cultures, where fewer constraints are imposed by the behavior of adjacent cells, the correlated (co-moving) area shrinks (fig. 30e).

Our statistical characterization of various endothelial cells revealed that monolayers move in locally anisotropic, 50-100 μm wide and 200-300 μm long streams. The variety of cells is an indication that the mechanism responsible for this behavior might be a universal property of cell cultures. As no apparent correlation is found in the position or direction of the forming streams, the phenomenon is most probably an emerging collective behavior, and the explanation is in the behavior of the individual cells.

Cell density clearly plays and important role, as in low density cell cultures, cells in front of a moving cell tend to move in similar direction, but cell movements in lateral directions are uncorrelated. Despite the presence of streams, cell mixing is substantial in the monolayers: with a good approximation, movement of adjacent cells can be considered as independent. Trajectory analysis revealed that the persistence of the individual cell motion is substantial, cells perform persistent random walks. Therefore, a minimal model explaining this behavior could be self-propelled cells with volume exclusion.

4.2. Self-propelled cellular Potts model

Active cell motion

Active cell motility involves cell polarity, a morphological, dynamical and biochemical difference between the cell's leading edge and tail [48, 49]. Thus, self-propulsion is modeled by first assigning a cell polarity vector $\mathbf{p}_k$ to each cell k. In the CPM, the probability of those elementary conversion steps that advance the cell center in the direction parallel to $\mathbf{p}_k$ is increased as

$$w(\mathbf{a} \to \mathbf{b}) = P \sum_{k=\sigma(\mathbf{a}),\sigma(\mathbf{b})} \frac{\Delta\mathbf{r}_k(\mathbf{a} \to \mathbf{b})\mathbf{p}_k}{|\mathbf{p}_k|}. \tag{4.5}$$

Parameter P sets the magnitude of the bias and $\Delta\mathbf{r}_k$ represents the displacement of the center of cell k during the elementary step $\mathbf{a} \to \mathbf{b}$.

The cell polarity vector is an attempt to represent the localization and magnitude of the biochemical changes characterizing the leading edge of a migratory cell. The unit vector rule in eq. 4.5 is supported by the ability of cells to spontaneously build up a polarization reacting to slight fluctuations of external cues [48]. A feedback mechanism in the cell regulatory network is a possible explanation of this behavior [30]. Cell displacement in turn controls the changes in the polarity vector in the model, as we assume that polarity is reinforced by locomotion and weakened without it. The molecular mechanism for cell polarity reinforcement by cell motility may involve either the stabilization of PIP_3 accumulation by actin polymerization [102, 83, 11], or the activation of Rac by microtubule dynamics [104, 80]. Therefore, in each MCS the change in $\mathbf{p}_k$ is

$$\Delta\mathbf{p}_k = \frac{\mathbf{p}_k}{T} + \Delta\mathbf{r}_k, \tag{4.6}$$

where T is the characteristic memory length, or persistence time of the polarization vector, and $\Delta\mathbf{r}_k$ is the displacement of the center of cell k during the MCS considered.

Rules set by eq. 4.5 and 4.6 together constitute a positive feedback loop. In this model, steric constraints may result in co-migration of adjacent cells as the retraction of one cell allows for the expansion of the other. The resulting expan-

sion of cell bodies (like the actin polymerization process in real cells) therefore can alter and synchronize cell polarity.

Model behavior

Model simulations with $N = 1000$ cells were performed in a 200 $\times$ 200 lattice with closed boundary conditions. Typical parameter values used were $\alpha = 2$ (surface energy of cell-cell contacts), $\lambda = 1$ (inverse compressibility) and $P = 2$, T =5 MCS. Parameter β is irrelevant in monolayer simulations as no free cell surfaces are present. After scaling by temperature, these parameters are within the same range as those in previous studies [32, 58, 69, 3].

The spatial scale of the model is again easily determined by comparing the empirical and simulated cell sizes. The target cell area was set to 50 lattice sites, yielding a distance of about 7 sites between cell centers in the monolayer. This compares to the experimentally observed 35 μm closest neighbor distance (see fig 28c), calibrating one lattice site to 5 μm. The duration of a MCS is calibrated by comparing empirical and simulated cell speeds (see below) resulting in one MCS to correspond to one minute, a value similar to the ones used in other CPM studies [58, 3].

Individual cells perform a persistent random walk Model simulations of single cells were performed with Potts parameters $\beta = 1$ and $\lambda = 1$ (the parameter α is irrelevant under these conditions). Fig. 32a reveals that in the absence of active motility ($P = 0$) the average displacement $D(t)$ grows with time t as

$$D(t, P = 0) \sim \sqrt{t}. \tag{4.7}$$

Thus, as in the original CPM [76, 97], cell movement is diffusive for $P = 0$. Large values of P result in unrealistic cell shapes and behavior as the effect of the other constraining terms in expression 1.6 diminish. The active motility rules set by eq. 4.5 and eq. 4.6 with $0 < P < 4$ result in individual cells performing a persistent random walk: as fig. 32a and c demonstrate, the average displacements are well fitted by eq. 2.6 for $D(t, P) > 1$.

Fig. 32b reveals, that the speed of active motion, S, is proportional to P in

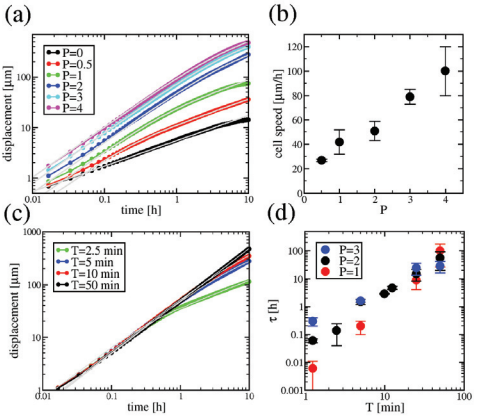

Figure 32: Motion statistics of individual, non-interacting cells in model simulations. (a): Average displacement, $D(t)$ versus time, t. Values of P are shown in the key, $\beta = 1$, $\lambda = 1$, $T = 5$min. Gray solid lines are fits by the persistent random walk formula (eq. 2.6) and a square-root function in case of $P = 0$. (b): The speed S of directed motion is set by parameter P. (c): Average displacement versus time curves and the corresponding fits, obtained from simulations with various polarization memory lengths. Values of T are shown in the key, $\beta = 1$, $\lambda = 1$, $P = 2$. (d): The persistence time of the random walk behavior, τ, mostly depends on parameter T through a non-linear relation, and to a lesser extent also on the active motion parameter P. [87]

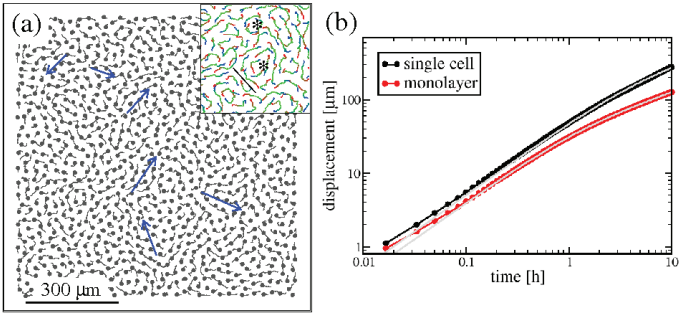

Figure 33: Motion characteristics in monolayer simulations. A representative parameter setting was chosen as $P = 2$, $T = 5$min, $\alpha = 2$, $\beta = 1$ and $\lambda = 1$. (a): Model cell trajectories from a 40 min long time interval reveal streams formed by several cells (blue arrows). The inset shows trajectories from a 90 min long interval, color-coded progressively from older to newer as red through green to blue. A shear-line separating streams moving in opposite directions (black line) and two vortices (asterisks) are indicated. (b): Average displacements of single, unconstrained cells are greater than those in a monolayer. Persistence time and cell speed in a monolayer fall from 40 to 30 minutes and from 55μm/h to 40μm/h, respectively. [87]

the $0 < P < 4$ range (parameter P is bounded by the connectivity constrains of the model). Because of the positive feedback between directed cell motion and maintenance of cell polarity in our model, the persistence time τ increases strongly both with P and the duration of the memory, T (fig. 32d).

Streaming behavior in monolayer simulations Monolayer simulations exhibit streaming similar to the experimentally observed, with shear lines and vortices present (fig. 33a). Motion of individual cells within the monolayer is somewhat hindered when compared to unconstrained cell motion, as the speed and persistence time decrease by 20% (fig. 33b). In addition to qualitative similarity, the calculation of flow fields allows a more rigorous comparison of model simulations to empirical data (fig. 34, to be compared with figs. 30 and 31). Lateral

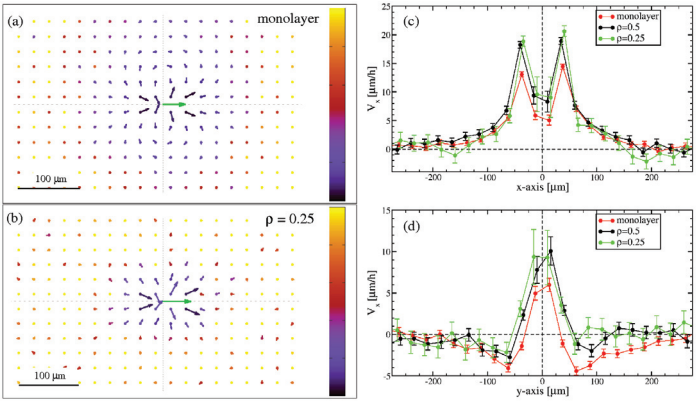

Figure 34: Flow fields $\mathbf{V}(\mathbf{r})$ around a moving cell within a monolayer (a) and a subconfluent culture (b) simulation. The corresponding parallel and perpendicular velocity profiles are shown in panels (c) and (d), respectively. In low density cultures correlations are reduced in the lateral direction. Cell density values specified in the keys are normalized to confluent culture density ($\rho = 1$). Velocity vectors represent one-hour-displacements, the green arrow indicates the average velocity of the cells. As in fig. 30, the color code in panels a and b indicates the estimated relative SEM, and the color scale represents the interval $[0 : 1]$. [87]

correlations and back-flow are reduced when non-adherent cells are simulated at lower cell densities (fig. 34b). At lower densities the average flow field still reveals the 'steric' repulsion of cells in the path of an actively moving cell.

Parameters Two new parameters, P and T, are introduced in addition to the usual CPM parameters α, β and λ. In monolayer simulations there are no free cell boundaries, therefore parameter β describing free cell surface energies is irrelevant. The model can also exhibit an ordered phase in which, responding to the closed boundary conditions, all cells participate in a single, system-wide rotational movement. This state is reached by increasing the memory duration T: increasing T or P in the streaming regime, streams become wider and longer (fig. 35a,e-h). Conversely, by decreasing either T or P, a diffusive state is recovered, where the persistence length is smaller than the size of a cell. In this limit $\mathbf{V}(\mathbf{r})$ is well approximated by the flow field of an incompressible fluid around a moving disk: V_x decays as x^{-2} and $-y^{-2}$ along the x and y axes, respectively.

The D_2 separation of adjacent cell pairs, when plotted against the mean cell displacement D (fig. 35b and d), reveals the system-wide ordered flow, when cells can cover large distances without changing their neighbors ($D \gg D_2/\sqrt{2}$). In the streaming regime the asymptotic relation described in eq. 4.4 holds indicating uncorrelated motion within the monolayer.

Depending on the values of P and T, increasing α can result in a multitude of changes. Reflecting its definition, a simulation with higher α values yields cells with smoother boundaries (figs. 36b and d). In general, reducing the freedom of cell boundary movement hinders cell intercalation, and thus movement within a monolayer, as indicated by decreasing speeds with increasing α. However, if self-propulsion is strong enough, the reduced intercalation can also yield wider streams as demonstrated by figs. 36c,e and f.

The above defined self-propulsion model is thus capable of explaining most experimental observations presented in section 4.1. Furthermore, the relatively simple model structure allows a thorough mapping of the parameter space. Even this simple representation yields individual cell speeds, persistence times in the correct range as well as a collective behavior comparable with the observed streaming. In particular, $T = 5$ minutes is a plausible value for the time needed to alter

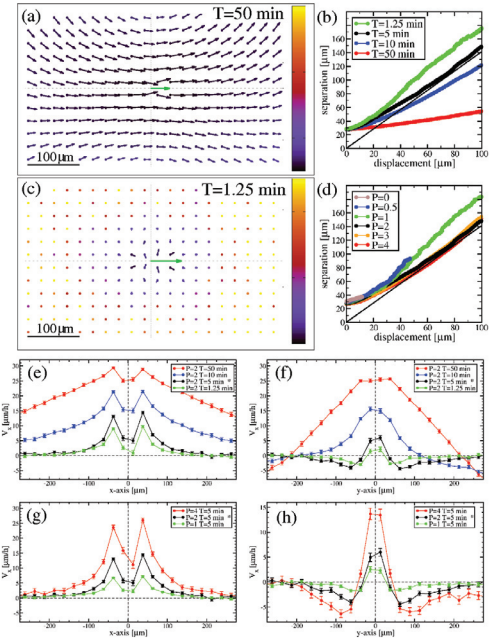

Figure 35: Self propulsion parameters P and T play a crucial role in defining the collective behavior of the monolayer. Flow fields $\mathbf{V}(\mathbf{r})$ are shown for long (a: $T = 50$min) and short (c: $T = 1.25$min) memory duration of cell polarity. The remaining parameters are the same as in fig. 33. Flow fields are presented as in fig. 34. The corresponding parallel and perpendicular velocity profiles are shown in panels (e) and (f), respectively. Increasing T results in wider, longer and faster streams. Similar, but less dramatic tendencies are seen when changing P (panels g and h). For large enough T, the system organizes into a phase where the correlation length is comparable to the system size. Movement within the monolayer is diffusive in the streaming regime as the average neighbor separation versus cell displacement curves (panels b and d) are consistent with the asymptotic behavior of eq. 4.4, shown as the solid line. In the globally ordered (rotating) regime cells move further without separating. The asterisk marks the parameter values used in fig. 33. [87]

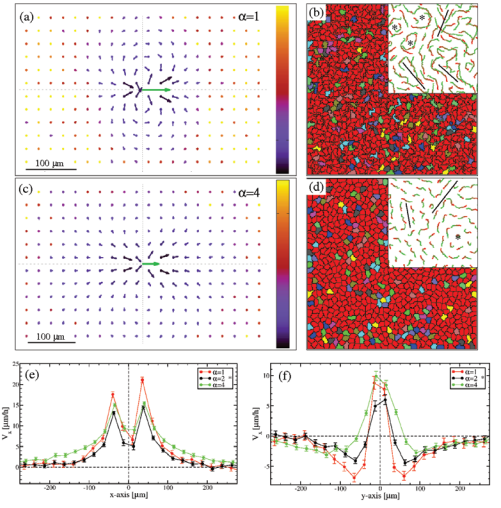

Figure 36: Role of cell adhesion parameter α. Simulation results are compared for $\alpha = 1$ (panels a, b) and $\alpha = 4$ (panels c, d). Self-propulsion is strong ($P = 3$), while the remaining parameters are the same as in fig. 33. As the configurations demonstrate (panels b, d), parameter α controls cell shape and cell boundary smoothness. The $\mathbf{V}(\mathbf{r})$ flow fields (panels a, c) and their profiles along the parallel (e) and perpendicular (f) axes reveal, the streams get wider with increasing α as cells cannot easily intercalate. Flow fields are presented as in fig. 34. The insets in panels (b) and (d) demonstrate cell trajectories, comparable with similar plots in figs. 30 and 33. The asterisk marks the parameter values used in fig. 33. [87]

cell polarity. With this value, it is possible to obtain cell speeds in the range of 20-40 μm/h within monolayers and 50 μm/h for individual cells. Our empirical data show cell speeds between 10 and 30 μm/h for monolayers. A similarly close, and independent agreement is obtained for the persistence times τ, at approximately one hour both in the model and in the experiments. The spatial structure of streams is strongly anisotropic, being approximately 200-300 μm long and 100 μm wide in both the experiments and in the simulations.

4.3. Discussion

Motion of polarized cells in high density While correlated cell velocities and streams in MDCK and HUVEC monolayers were recently reported [37, 101], their dynamics remained largely unexplained. To obtain further empirical data to test our model, we systematically investigated monolayer cultures of three different endothelial cell lines. Our finding, that 5-20 cells move together in narrow, chain-like groups, is in accord with previous reports. Because our cultures were grown in a monolayer, our measured cell speeds and persistence times ($S \approx 10-30\mu$m/h, $T \approx 1$h) somewhat differ from the values previously reported for individual endothelial cells ($S \approx 40\mu$m/h, $T \approx 3$h [85]; $S \approx 50\mu$m/h, $T \approx 0.6$h [47]).

Models for collective cell movements Previous theoretical studies on cell movement include a multi-particle model that was proposed to explain the collective migration of fish keratocytes [90]. In that study long-range ordered and disordered states were reported, but no streaming behavior. The model included short range repulsion and long-range attraction between the particles within a certain range (not necessarily between neighbors), as well as self-propulsion and the alignment of the propulsion direction towards the actual displacement of the particles.

Another theoretical study, which did not have the aim to describe cells, investigated a 2D system of self-propelled particles with short range repulsive and intermediate range attractive interactions, as well as an alignment of the motion direction to the local average [35]. In this model, the interaction was restricted to Voronoi neighbors, but the velocity alignment rule probably prevented the development of narrow streams. Although this study did not predict the particular

streaming modes of collective cell sheet motility, it showed that such systems can exhibit six phases: gas, fluid and solid phases both with and without long-range ordered movement.

The model proposed here for streaming in cell monolayers is based on the CPM, and includes a more plausible representation of cell polarity and active cell motility than the rule variants involving direction alignment to the local average direction of motion [100, 35, 4].

Beltman et al. [5] studied a very similar problem in a three dimensional lymph node, where T cells were shown to organize into streams. The presented model of a lymph node contains extracellular matrix fibers and more complicated assumptions about cell motility – thus the resulting model complexity prohibited an exhaustive analysis of model assumptions and parameters.

In this study the focus is on the collective cell behavior in a simple two dimensional environment, where the feedback between polarity and cell motion is represented by a simpler and more transparent model. These simplifications allow us to map the resulting model parameter space systematically, explain most of the observed behavior and compare the model with experimental data using a variety of quantitative and qualitative measures.

Positive feedback between polarity and cell motility The positive feedback between cell polarity and cell displacement is also supported by careful analysis of individual cell migration paths [79]. That study proposed a number of stochastic models for cell center speeds, the simplest of these models being a generalization of the OU process,

$$\frac{d\mathbf{v}}{dt} = a\mathbf{v}^* - b\mathbf{v} + \sigma(\mathbf{v})\xi \tag{4.8}$$

and

$$\frac{d\mathbf{v}^*}{dt} = a\mathbf{v} - c\mathbf{v}^*, \tag{4.9}$$

where $\mathbf{v}$ is the cell speed, $\mathbf{v}^*$ represents self-propulsion, ξ is an uncorrelated

noise with a velocity-dependent variance $\sigma(\mathbf{v})$, and a, b, c are parameters. In this stochastic particle model, the update of the $\mathbf{v}^*$ self-propulsion term is analogous to our rule set in eq. 4.6.

A variant of the model was also investigated in which the actual elementary step, and not the displacement of the center of mass, is compared with the polarity vector as

$$w(\mathbf{a} \to \mathbf{b}) = P \sum_{k=\sigma(\mathbf{a}),\sigma(\mathbf{b})} \frac{(\mathbf{b}-\mathbf{a})\mathbf{p}_k}{|\mathbf{p}_k|}. \tag{4.10}$$

Simulations using eq. 4.10 instead of eq. 4.5 also resulted in similar overall behavior. Thus, model behavior does not depend on the details how the feedback between cell polarity and motility is represented.

A recent high-throughput study of the genes involved in endothelial sheet migration [101] identified clusters of genes that effect mostly either the active motile activity of cells (analog to parameter P), or a directional migration response into an area stripped from cells (not included in the present model), or cell-cell coordination. Unfortunately, the PI3K/PTEN mechanism we considered here as a possible molecular feedback system capable of providing both persistent motility and cell-cell coordination, was not tested directly in that study. Si-RNA knockdown of the PTEN protein resulted in somewhat reduced cell velocities and cell-cell coordination within the confluent sheet. This change is compatible with PTEN playing a role in determining cell polarity in this experimental setting. However, unpredicted by single cell studies performed in non-endothelial systems, loss of the PTEN protein also resulted in a marked increase in sensitivity (enhanced directional migration) towards the denuded area. Thus, while a modular structure of cell motility regulation, including cell polarity, was empirically supported, the molecular machinery underlying coordinated cell movement remains an intriguing problem to study.

Even less molecular details are known about what drives changes in cell polarity in the absence of external cues such as chemoattractant gradients. However, in a motile cell the polarization direction must change eventually. For instance, when the advance of the leading process is impaired and the process collapses, a new migration direction is selected and cell polarity is altered.

Surface tension and intercellular adhesion Surface energy-like parameter β of a three-dimensional cell aggregate has been shown to be proportional to the cadherin density at the cell-matrix surface [25, 38]. Despite this evidence, it is still surprising that the analogy between liquid droplets and cell aggregates is good enough to describe the surface roughness of individual cells. Such a relation was demonstrated, at least for the surface cells of tumor spheroids by Hegedüs et al. [38]: the membrane of the outermost cells were found to be smoother when the cadherin expression was higher.

It is less clear if a similar relation holds in two dimensions between cadherin density and the surface energy-like parameter α, associated with cell-cell contacts. If there is a similar correlation between the roughness of the cell-cell contact surfaces and adhesion molecules, then the results presented in fig. 36 are also consistent with recent findings, indicating that the correlation in cell movements is reduced when VE-Cadherin, mediating intercellular adhesion between endothelial cells, was silenced [101].

5. Multicellular sprout formation

Sprouting, the collective movement of cell chains, is of great importance during development and in certain diseases such as tumor growth [26, 60]. Observations of vasculogenesis in vivo indicated that early vascular network formation includes sprouting, the extension of linear segments containing multiple cells [77]. This process is markedly different from the gradual coarsening of an initially uniform density field, and its possible arrest, characteristic for colloid gels (see, for instance Foffi et al. [21]). In vitro culture conditions yield sufficiently high resolution to trace the motion of individual cells during the patterning process. Sprout expansion involves cell motility guided by adjacent projections of other cells or elongated multicellular structures.

Multicellular sprouting is often considered as a special case of sheet migration, the expansion process of a monolayer into an empty area or "wound". During sheet migration cells at the boundary exert substantial traction forces [17] and are thought to pull the passive bulk of the sheet forward [13]. Similarly, cells participating in sprout formation are often divided into two subpopulations and the process is explained as *leader-* or *tip cells* pulling a gliding bulk of passive, *stalk cells* by means of cell-cell adhesion [26]. The assumption that the stalk population is not participating in active cell motion is based on observations indicating that these cells have few connections with the extracellular matrix (ECM) environment [26], or lack filopodia [31].

The above view is, however, inconsistent with the widely accepted models of cell-cell adhesion. In particular, cadherin-mediated cell-cell adhesion has been repeatedly shown to be analogous to surface tension [23, 22, 7, 25, 38], and has been modeled accordingly in theoretical studies [32, 42, 66]. Surface tension-stabilized structures are, however, prone to the Plateau-Rayleigh instability: a column of liquid with a circular cross-section should break up into drops if its length exceeds its circumference [12, 41]. Due to this instability, as we demonstrate below, a sprout pulled by a leader cell should also break up. Therefore, multicellular sprouting cannot be fully accounted for by the presence of leader cells and cell-cell adhesion alone. While stalk cells may be detached from the matrix, their motion should not be entirely passive: an active cell-guided motility

might be present, which invalidates the tissue-fluid analogy and the arguments for the Plateau-Rayleigh instability do not apply.

In the previous sections, motility analysis of certain cell cultures indicated that the elongated (stalk) cell surfaces are more attractive migration targets than the surfaces of well-spread cells in the aggregate bulk. However, this mechanism proved to be insufficient to adequately reproduce multicellular sprouting from a reservoir of adherent cells, when investigated with computational simulations. The movement of the sprout tip is not sufficiently persistent resulting in curved branches, and the previously formed sprout bodies move sideways. Furthermore, the speed of sprout expansion decreases over time.

In this section a cell-autonomous mechanism (i.e., a mechanism independent of extracellular chemical or mechanical guidance fields) for multicellular sprouting is explored that utilizes both the leader-cell concept and the preferential attachment of cells to elongated neighbors, discussed previously.

5.1. Empirical findings

In experimental systems, where sprouting activity has been analyzed in detail, active and passive cell states can be, indeed, distinguished based on the degree of cellular motility. During the formation of the early vasculature in quail embryos clusters of non-motile cells are maintained while highly motile multicellular sprouts invade avascular areas [77, 10]. In mouse allantois explants rapidly migrating sprout precursor cells appear within a cluster of cells lacking autonomous motility [72]. In cultures of C6 cells linear branches contain highly motile cells whereas cells remain non-motile in the well-spread, isotropic clusters (fig 13).

By analyzing published image sequences, in fig. 37 we demonstrate that the speed of sprout expansion is constant in each of these cases. Furthermore, the sprout is often surprisingly “fluid”: cells move with different velocities and thus the order of cells within the sprout can be changed.

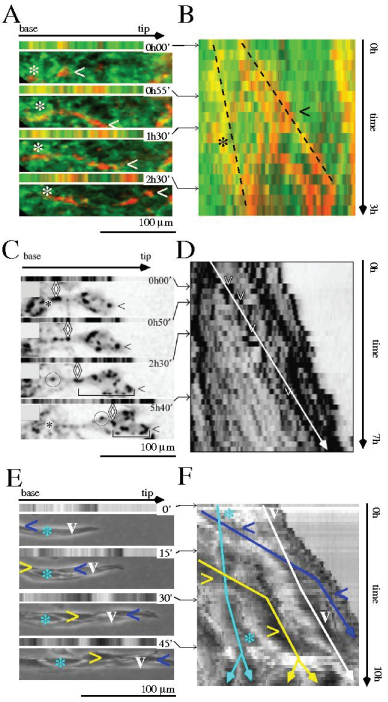

Figure 37: Multicellular sprout expansion in three experimental systems. Panels A, C and E show cell configurations at various time points. Panels B, D and F show the corresponding kymograms: intensity profiles along the linear structure for each frame recorded, therefore, in these plots moving objects appear as tilted lines. Tip cells are marked with a caret (<), while an asterisk (*) denotes a cell at the approximate position of the sprout base. The expansion of the sprout is linear in time in all three systems. A,B: QH1-labeled endothelial cells (red) form a vascular segment during vasculogenesis in a HH stage 7 quail embryo (data re-analyzed from Czirok et al. [10]). Surrounding tissue movements are visualized by changes in the ECM component Fibrillin-2 (green). The area shown in panel A co-moves with the surrounding ECM. C,D: CD34-labeled cells of a mouse allantoic explant (after Perryn et al. [72]). A cell moving from the middle of the sprout to the tip is marked with a diamond. E,F: expansion of a two-cell-wide linear sprout in cultures of C6 cells (data from fig. 13). The initial tip cell (marked 'v') is taken over by a faster migrating cell (marked '<'). The latter cell slows down after reaching the tip, and thus the overall sprout elongation speed remains unchanged. [86]

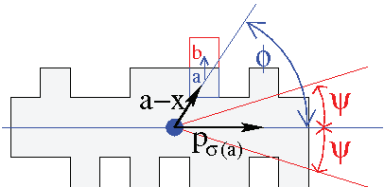

Figure 38: Cell polarity vector and an elementary step. In the elementary step depicted (blue arrow) the site index $\sigma(\mathbf{a})$ at lattice site $\mathbf{a}$ is copied to site $\mathbf{b}$, resulting in the expansion of cell $i = \sigma(a)$. The probability of the $\mathbf{a} \to \mathbf{b}$ step depends on both its location and direction. According to eq. 4.5, the direction $\mathbf{b} - \mathbf{a}$ is projected onto the normalized polarity vector of the cell, $\mathbf{p}_i$. Membrane fluctuations at the front of the cell are increased by eq. 5.1 and are attenuated elsewhere. The width of the leading edge is 2ψ radians, measured from the cell's center of mass ($\mathbf{r}$, blue dot) and polarity vector direction $\mathbf{p}_i$. As the elementary step considered is at site $\mathbf{a}$, the angle between $\mathbf{a} - \mathbf{x}$ and $\mathbf{p}_{\sigma(\mathbf{a})}$ is ϕ. [86]

5.2. Self-propelled cellular Potts model with tip cells

Definition

The effect of the elementary step specific bias w in eq. 1.8 is now constructed as the sum of three different effects, described as $w_1 + w_2 + w_3$. The effects are: (w_1) cell polarization and the resulting persistent directional motility as in eq. 4.5, (w_2) a novel term, introducing non-uniform membrane dynamics along the cell perimeter, and (w_3) the preferred attachment to elongated cells as in eq. 3.8.

Cell polarity has an effect on the cellular shape changes as membrane dynamics is more pronounced at the leading edge and inhibited at the sides and trailing edge [49]. Thus, if ψ is the half-width of the leading edge, $\mathbf{p}_{\sigma(\mathbf{a})}$ is the polarity vector of cell $\sigma(\mathbf{a})$ (which contains lattice site $\mathbf{a}$, see fig. 38), we assume

$$w_2(\mathbf{a} \to \mathbf{b}) = S_{\sigma(\mathbf{a})} f(\psi - \phi(\mathbf{p}_{\sigma(\mathbf{a})}, \mathbf{a} - \mathbf{r}_{\sigma(\mathbf{a})})). \tag{5.1}$$

In eq. (5.1) S_k sets the magnitude of this effect for cell k, $\phi(\mathbf{u}, \mathbf{v})$ denotes the absolute value of the angle between the vectors $\mathbf{u}$ and $\mathbf{v}$, and $f(\alpha) = 2\Theta(\alpha) - 1$ is conveniently constructed using a Heaviside function $\Theta(\alpha)$. Notice, that w_2

depends only on $k = \sigma(\mathbf{a})$, the expanding cell.

Simulation results

Simulations were initiated from compact aggregates of 25-50 cells. The linear system size, $L = 300$, was chosen as sufficiently large to allow sprout extension without interaction with the boundaries.

The 8 parameters which describe the behavior of model cells are α (cost associated with cell-cell contacts), β (cost associated with free cell surfaces), λ (cell stiffness parameter), P (self-propulsion activity), T (polarity vector memory length), S (coupling between boundary activity and cell polarity), ψ (half-width of the leading edge) and γ (preference for elongated cells). The first three of these defines the basic CPM [32], P and T is a representation of active cell motility analyzed in detail in the previous section. Parameters S and ψ correspond to the specific cell behavior patterns modeled here.

Since the cell population to be modeled is homogeneous, the same set of parameter values are assigned to each cell. The only exception is the persistence time, which is used to distinguish leader and passive cells: the polarization of passive cells is assumed to decay almost instantaneously ($T_{passive} = 1$ MCS), while the polarization is quite persistent in leader cells ($T_{leader} = 500$ MCS). Polarization, therefore, has no substantial effect on the motion of passive cells: they lack directed motion and perform a random walk in the absence of cell-cell interactions.

The stiffness parameter λ does not play a role in the sprouting processes considered here, therefore it is fixed at $\lambda = 1$. However, the surface energy-like quantities α and β are important: their magnitudes set the flexibility of cell interfaces. As the chance for a spontaneous fluctuation (the creation of a one-lattice-site bulge) at the free cell boundary is $\exp(-2\beta)$, we considered values in the range $0 < \beta \leq 6$ and $\alpha \in \{1, 2\}$, in accord with the literature [76, 2, 3].

Passive cell-cell adhesion alone is insufficient to maintain cell supply to expanding sprouts To investigate the mechanism proposed in the literature – an active tip cell pulling the passive bulk to form a sprout – only the active motion

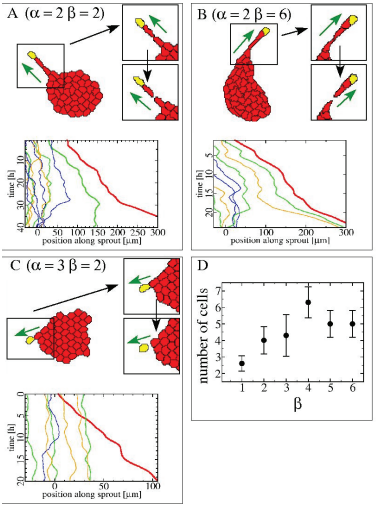

Figure 39: Leader cells are unable to sustain cell recruitment to the sprout from the initial aggregate by cell-cell adhesion alone. In the simulations tip cells eventually detach from the sprouts – as shown in the insets – irrespective of surface tension parameters. Green arrows mark the direction of sprout extension, black arrows indicate time-sequence. The self-propulsion parameter P was set to yield minimal sprout elongation speeds. Trajectory plots in each panel show cell center movements along the sprout axis. A, B: low and high costs associated to free cell boundaries ($\alpha = 2, \beta = 2, P = 2$) and ($\alpha = 2$, $\beta = 6$, $P = 7$), respectively. Larger β values result in a thick initial bulge and longer sprout extension. Passive cells retract after the sprout breaks – a process driven by the elastic energy accumulated in the sprout. C: An increased cost associated to cell-cell boundaries (α) results in smoother and shorter contact areas ($\alpha = 3$, $\beta = 2$, $P = 1$). Due to the reduced contact surface cell-cell connections break more easily. D: The number of cells incorporated in the sprout at its maximal extent was determined for $\alpha = 1$ and various values of the parameter β. All data points are an average obtained from three independent runs, the errorbars represent standard deviations. [86]

and the selective membrane fluctuation mechanism is used, the preferential adhesion term is set to zero ($w_3 \equiv 0$). Simulations were performed with leader and passive cells for a wide range of the CPM parameters α and β; thus controlling the flexibility of cell-cell and free cell boundaries, respectively (fig. 39).

The ability of a leader cell to pull a sprout depends on the interplay between the surface tension of the aggregate, β, and the propulsion strength P. For large enough β the increase in the perimeter of the area encompassed by the cell blocks the forward movement of the sprout tip. On the other hand, if the propulsion strength P is too large, the tip cell moves too fast for the passive cells to respond. Thus, for each set of CPM parameter values we determined the lowest propulsion strength P_{min} that still leads to a (slow) sprout expansion.

In simulations performed with minimal sprout expansion speeds the leader cell deforms the shape of the aggregate and pulls a few passive cells into the forming sprout. Then, the sprout length is increased at the expense of its width – reminiscent to the reported dynamics of tracheal tube formation in fruit flies Montell [60]. However, after the sprout has sufficiently narrowed, cell-cell connections break: passive cells are pulled back to the initial aggregate leaving the leader cell, and possibly a few passive cells, in a separate cluster. As fig. 39d demonstrates, the sprout at its maximal length contains 3-4 cells on average.

The maximum sprout length increases with β (the penalty associated with free cell surfaces) and slightly decreases for increasing α. The decrease in α allows for longer, more interdigitated and hence stable cell-cell contacts. Increasing the surface tension of the cell clusters (β) yields more compact aggregates and thicker sprout bases. When $\beta < \alpha/2$, cells dissociate from the aggregate and diffuse freely on the substrate.

The inability of surface tension to maintain a sprout can be discussed by simple geometrical arguments. Due to the similarity between cell-cell adhesion and surface tension [22] we only need to compare cell perimeter lengths and their associated CPM "Hamiltonian", u (see eq. 1.6), in a long sprout of width d and at a surface of an aggregate (fig. 40). For simplicity we consider only rectangular cells at their target area A, but the argument can be easily extended to more complex

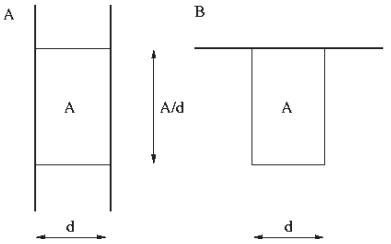

Figure 40: Comparison of cells in two configurations. A cell of width d within a linear sprout (A) and a similar cell at the surface of an aggregate (B). Thick and thin lines represent free and cell-cell boundaries, respectively. [86]

shapes. A cell located at the surface of an aggregate contributes

$$u_{surface}(d) = \frac{A\alpha}{d} + (\alpha/2 + \beta)d \tag{5.2}$$

to the CPM Hamiltonian, as borders between cells are accounted for twice. Since a cell at the surface can adjust its width to minimize u, its contribution becomes

$$u_{surface} = \sqrt{2A\alpha(\alpha + 2\beta)}. \tag{5.3}$$

In contrast, the width of a cell in a sprout is set by the sprout thickness, and the corresponding contribution to u is

$$u_{sprout}(d) = \frac{2A\beta}{d} + \alpha d. \tag{5.4}$$

If $\beta > \alpha/2$, it is easy to show that for arbitrary d:

$$u_{sprout}(d) \geq 2\sqrt{2A\alpha\beta} > u_{surface}. \tag{5.5}$$

Thus, a cell always prefers to be at the surface of an aggregate, rather than in a sprout – which blocks surface-tension driven cell recruitment at the sprout base.

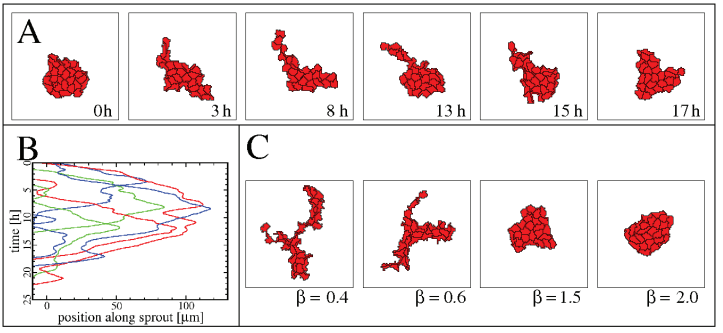

Figure 41: Spontaneous sprouting without leader cells. A: time-course of sprout growth. Several elongated cells form a several cell-diameter long, transient sprout ($\alpha = 2$, $\beta = 1$, $P = 4$, $\gamma = 5$). The lifetime of the sprout is ≈15 hours. B: cell movements in the sprout shown in panel A are depicted as trajectories. C: the surface energy of free cell boundaries (β) is a key determinant of sprout shape. High values of β keep the cells together in the initial aggregate. Lowering β increases cell surface fluctuations and cells can break away from the aggregate more frequently ($\alpha = 2$, $P = 4$, $\gamma = 5$). [86]

Spontaneous sprout formation in a model with preferential attachment to elongated cells Previously we showed that sprouts could be stabilized by preferential attraction to elongated cells (see for instance fig. 20 or fig. 22). As $w_3 \neq 0$, the dynamics of the whole system is not a surface tension-driven relaxation process towards equilibrium. However, the motion of a single cell in a given environment is still governed by effective surface energies. The lower effective surface energy (α) values associated with contacts on elongated cells in the sprout decreases expression 5.4, therefore, the preferential attraction to elongated cells can offset the penalty for long free boundaries, and thus invalidate the instability condition in eq. 5.5.

In similar systems, without leader cells, but with $w_i \neq 0$ for $i = \{1, 2, 3\}$, random fluctuations in cellular motility can initiate spontaneous sprouts by displacing a cell from the aggregate (fig. 41). Since the displaced cell continues to attach to the aggregate, it assumes an elongated shape which attracts additional cells into the sprout. This spontaneous sprouting process - without specialized leader cells - is heavily influenced by the strength of surface tension β. If the surface tension is low, free cell surfaces fluctuate more and it is easier for the cells to leave the aggregate. Thus, the unrealistic jagged appearance of cell surfaces is related to the possibility that such sprouts can develop. Furthermore, irrespective of the surface tension strength, long sprouts cannot be maintained without the tip's attachment to another group of cells. The jagged sprout surfaces and their limited lifetime, however, does not match the experimentally observed structures and dynamics shown in fig. 37.

Leader cells and preferential attraction The unrealistic cell shape and sprout behavior that emerge from the simulations shown in fig. 41 are partially the consequences of ignoring some basic properties of cell motility, such as localized protrusion activity in the front of the cells or directional persistence of cell motility. Furthermore, the motile state of cells in the sprout is clearly different from those in the aggregate, thus it is reasonable to include leader and passive cells in the model.

Simulations with leader cells ($P = 4$, $T = 500$MCS), preferential attraction to elongated cells ($\gamma = 3$) and localization of membrane protrusions to the leading

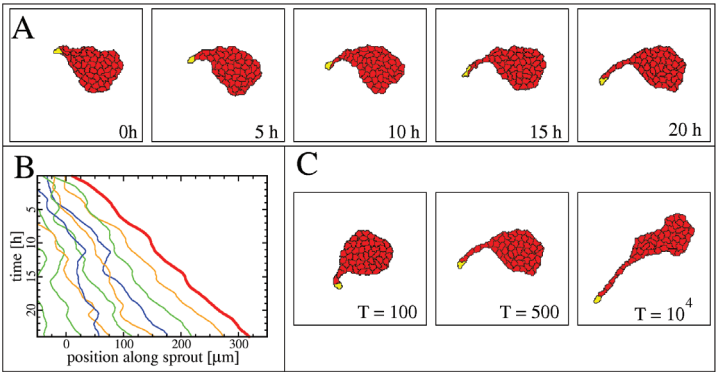

Figure 42: Leader cell initiated sprouting behavior in a system with preferential attraction to elongated cells. A: typical time-course of sprout growth: the leader is slightly elongated, thus it pulls passive cells from the initial aggregate. The passive cells become elongated as well and attract further cells into the growing sprout. With sufficient supply of cells, the expansion can continue for an extended time period ($\alpha = 2$, $\beta = 2$, $P = 4$, $T = 500$MCS, $\gamma = 3$, $S = 2$, $\psi = 0.1$). B: cell trajectories along the sprout direction reveal cells entering the sprout as well as changes in cell order due to differential motion in the sprout. C: persistence time of polarity defines sprout shape and length, through the polarity persistence parameter T. When the leader cell is more persistent, longer and straighter sprouts form. [86]

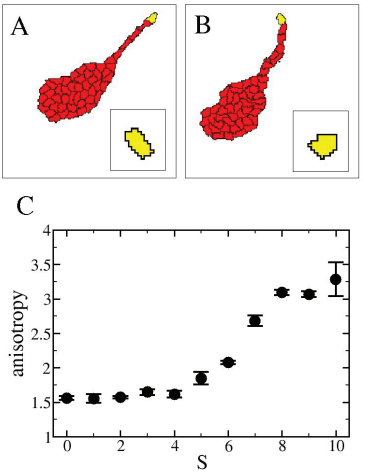

Figure 43: The effect of restricting elementary steps (membrane fluctuations) to the leading edge. A: for $S = 4$, $\psi = 0.1$, $P = 4$, motile cells are elongated (inset) which contributes to the sprouting process ($\alpha = 2$, $\beta = 2$). B: as a comparison, for $S = 0$ and $P = 4$ the disk-shaped cells recruit cells less efficiently resulting in slower elongation of the sprout ($\alpha = 2$, $\beta = 2$). C: the shape change of non-interacting leader-type cells is characterized by their anisotropy θ. [86]

edge ($S = 2$, $\psi = 0.1$) yield sprouting dynamics comparable to that of experimental results (fig. 42). Thus, leader cells are able to leave the initial aggregate, then form and maintain an expanding sprout by recruiting passive cells at the sprout base. The shape of the sprout as well as its expansion speed is determined by the persistence time of the leader cell. In particular, faster expansion increases cell elongation, which helps to recruit additional cells at the sprout base.

The effect of localizing the elementary steps to the leading edge is demonstrated in fig. 43. For $S > 0$, spin conversions at the leading edge are accepted more frequently. As a consequence, cells become elongated in the direction of their movement which enhances the recruitment of cells to the sprout.

5.3. Discussion

Sprouting is a collective cellular phenomenon exhibited by several types of tissue cells: avian vasculogenesis [77] and drosophila trachea formation [60] represent two well-studied examples during embryonic development. Collective chain migration is also ubiquitous during tumor invasion [26], as well as in cell cultures (both 3D [27] and 2D). Cell-cell contacts also seem to play a role in neural crest cell migration [91]. Thus, empirical evidence suggest that multicellular sprout formation is a general ability of a wide variety of tissue cells.

Tip and stalk cells

In sprouting experiments two subpopulations of cells is distinguished based on their motility properties and extracellular contacts: tip cells at the front of the sprouts and stalk cells constituting the sprout body [31, 43]. Tip cells connect to the environment with several filopodia and are thought to pull the trailing cells forward, whereas stalk cells lack filopodia and their attachment to the substrate is diminished [31, 26]. The mechanism of the tip cell selection is not yet clear, but might involve filopodia growth inhibition through the Delta-Notch signaling pathway: upon contact with the tip cell, the followers are inhibited and thus cannot grow filopodia to become a leader-type cell [6].

The inability of the stalk cells to produce structures needed for well established motion might be interpreted by the lack of cell polarization stability: to produce filopodia, actin polymerization has to be maintained for an extended time in the direction of cell polarity. If, however the polarity changes with a high frequency, there isn't enough time to complete the processes needed for sustained migration. Using this hypothesis, tip and stalk cells are distinguished based on their persistence time of cell polarity. The lack of empirical data, however, makes it difficult to directly measure the motion persistence of the specialized tip and stalk population.

Sprouting in silico

Sprouts in the model presented here are (i) able to recruit cells from the base, and (ii) are linear structures (iii) with a steady expansion speed. Furthermore, (iv) the

order of cells in the sprout is dynamic, cells can mix. Two main assumptions were made to achieve this behavior: (i) a special, persistently moving tip cell is present in the population and (ii) cells exhibit a preferential adhesion to elongated cells. The duration of cell polarity in leader cells, $T \approx 6h$ is long, however individual endothelial cells can exhibit a persistence time of several hours in low cell density culture [85].

Although cells may change their order in the stalk, in the current implementation of the model the role of the tip cell cannot be transferred or changed. Extending the model to contain a mechanism for the selection of tip cells would enable the investigation of this problem.

Sprouting without a leader

In previous sections, the model of network formation through preferential attachment produced sprouts in both the CPM and particle model formulation. Cells in these models behave as stalk cells, as they have little or no persistence of motion, which could explain the unrealistic growth profile, showing a decreasing speed and limited length. To better compare the models with and without tip cells, sprouting was investigated in the persistent CPM as well, where no tip cells were nominated. The sprouts resulting from a homogeneous population of stalk cells proved to be short lived and limited in size, similar to the previously observed, non-persistent CPM. In both cases the frequency and length of the spontaneous sprouts depends on the surface tension parameters.

Sprout-guidance is essential for sustained sprouts

Sprout elongation is likely to involve active cellular motility guided by cell-cell contacts, and cell surfaces in the sprout must be more attractive than surfaces of well-spread cells in the aggregate bulk. Here the preferential attachment hypothesis is utilized that take advantage of the elongated shape of stalk cells right after incorporation into the sprout. However, an alternative mechanism to distinguish sprout cell surfaces might also be the altered composition of cell surface-attached ECM fibers [27].

Passive cells, however, are unable to maintain sprouts, due to the coarsening

resulted by the effective surface tension. Based on the well-studied tissue-fluid analogy [23, 22, 7, 25, 38] passive cells attached by cadherins resemble fluid droplets and as such, they are not capable of maintaining a continuous column of liquid and break up into droplets. This behavior is also demonstrated with the self-propelled cellular Potts model (introduced in section 4.2.).

Other, widely considered sprout-guidance mechanisms involve chemotaxis [58, 2, 59, 3] or mechanotaxis probing the ECM environment [64, 62, 54, 78]. The latter, mechanistic model of vasculogeneis, assumes that cells exert mechanical stress on the underlying substrate, and the resulting strain guides cellular motility. Lateral migration of cells can also be limited by ECM fragments [27], ECM-bound guidance cues such as VEGF isoforms or semaphorins [39]. Cadherin-independent cell-cell adhesions, such as tight junctions are also expected to behave differently from the liquid droplet models, in which the relative movement between adjacent cell bodies is irrelevant as long as the size of their contact surface is preserved. The integration of these cellular mechanisms into a mechanistic model of sprout elongation, however, remains an exciting goal.

6. Summary

The self-organization of independent units into a non-trivial pattern or complex is a major phenomenon throughout developmental biology, from the sub-cellular level to tissues. In this study the formation of a multicellular structure is discussed, that eventually gives rise to the vascular network: the primary vascular plexus in warm-blooded animals.

In section 3., formation of multicellular linear segments and networks of various cell types are presented. We hypothesize that the mechanism behind this process is a preferential attachment to elongated cells. Analysis shows that close contact with elongated structures enhances motility. A cellular model is proposed in which cells (i) are adhesive, (ii) maintain a fixed size and (iii) have a preference to adhere to elongated neighbors. Simulations with a particle model and a cellular Potts model both predict a quasi stationary state in which network-like patterns similar to the experiments are produced, as revealed by the local anisotropy and structure factor of cell configurations. The characteristic pattern size in the models depend only slightly on the cell density above the percolation threshold, which is in good agreement with experimental findings.

Cells in this model perform a random walk and therefore sprout growth is decreasing in time. In section 4. a polarization mechanism is suggested for motile cells: polarization is maintained by successive displacements and diminished otherwise. In turn, cell movement in the direction of polarization is enhanced, creating a feed-back loop between the two systems. This formulation reproduces the collective streaming motion of endothelial cells in a monolayer, as well as the motion of individual cells.

In section 5. the concept of a leader cell is introduced to better describe sprouting. We hypothesize that leader cells differ from other cells solely in their motion persistence. We show that maintenance of long sprouts is not possible in the widely accepted view of sprouting which describes the process as the actively moving leader cell dragging the passively gliding followers. Cells with preferential adhesion and a persistent leader are, however, producing realistic sprouts and therefore represent a new model for vasculogenesis.

7. Összefoglalás

A fejlődésbiológiában fontos szerepet játszik az önszervező mintázatképződés a sejt alatti mérettartományoktól egészen a szöveti és az egész szervezetre kiterjedő méretekig. Jelen dolgozatban a sejt és a szövetek méretskálája között kapcsolatot teremtő ilyen önszerveződést vizsgálunk: a melegvérű élőlényekben létrejövő elsődleges érhálózat kialakulását.

A 3. fejezetben több sejttípus sejtlánc- és hálózatképzését mutatjuk be. Feltevésünk szerint ezen viselkedés egy lehetséges magyarázata a sejtek preferenciális adhéziója elnyúlt szomszédaikhoz. Az anizotrópia hatása a sejtmotilitásra kísérleteinkben is kimutatható. A hipotézist egy sejt-szintű modell segítségével vizsgáltuk, melyben a sejtek (i) adhezívek, (ii) véges térfogatot tartanak fenn, valamint (iii) szomszédaikhoz azok anizotrópiájával arányos mértékben vonzódnak. A modellt egy részecske- és egy sejt-szintű Potts modellel szimuláltuk. A szimulációk során létrejövő kvázi-stacioner mintázatok, azok kialakulása, továbbá sűrűség-függése is a kísérleti megfigyelésekkel jó egyezést mutatnak, amint azt a konfigurációk struktúrfaktora és lokális anizotrópiája is mutatja.

A modellben létrejövő sejtláncok növekedése, a kísérletileg megfigyelt állandó sebességgel szemben, idővel lelassul, ami a szimulált sejtek diffúzív mozgásával magyarázható. A 4. fejezetben egy új önhajtási mechanizmust javasolunk, melyben a sejt polarizációját a sejtmozgás gerjeszti és stabilizálja, mozdulatlanság esetén azonban exponenciálisan lecseng. A polarizáció irányában történő elmozdulást jutalmazzuk, így a polarizáció és a sejtmozgás egy pozitívan visszacsatolt rendszert alkot. A modell hűen adja vissza úgy az egyedi sejtek mozgását, mint az összefüggő sejtrétegekben megfigyelt áramlástereket.

A nyúlványképzés pontosabb leírása végett az 5. fejezetben bevezetjük a vezérsejt koncepcióját: feltételezzük, hogy a vezér-sejt csupán mozgásának perzisztenciájában különbözik a többi sejttől. Megmutatjuk, hogy az általánosan elfogadott kép, miszerint a vezér-sejt pusztán a sejt-sejt adhézió segítségével húzza maga után passzív követőit, nem képes elegendően hosszú és stabil nyúlványokat létrehozni. A preferenciális adhézióval rendelkező sejtek azonban a létrejövő nyúlványok időfejlődését és stabilitását is helyesen adják vissza, így az általunk javasolt modell az érhálózatképzés egy merőben új magyarázatát adhatja.

Bibliography

[1] W. Alt. Biased random walk models for chemotaxis and related diffusion approximations. *J Math Biol*, 9(2):147–177, Apr 1980.

[2] Amy L Bauer, Trachette L Jackson, and Yi Jiang. A cell-based model exhibiting branching and anastomosis during tumor-induced angiogenesis. *Biophys J*, 2007. doi: 10.1529/biophysj.106.101501. URL http://dx.doi.org/10.1529/biophysj.106.101501.

[3] Amy L. Bauer, Trachette L. Jackson, and Yi Jiang. Topography of extracellular matrix mediates vascular morphogenesis and migration speeds in angiogenesis. *PLOS Comp. Biol.*, 5:e1000445, 2009.

[4] Julio M Belmonte, Gilberto L Thomas, Leonardo G Brunnet, Rita M C de Almeida, and Hugues Chaté. Self-propelled particle model for cell-sorting phenomena. *Phys Rev Lett*, 100(24):248702, 2008.

[5] Joost B Beltman, Athanasius F M Marée, Jennifer N Lynch, Mark J Miller, and Rob J de Boer. Lymph node topology dictates t cell migration behavior. *J Exp Med*, 204(4):771–780, Apr 2007. doi: 10.1084/jem.20061278. URL http://dx.doi.org/10.1084/jem.20061278.

[6] Katie Bentley, Holger Gerhardt, and Paul A Bates. Agent-based simulation of notch-mediated tip cell selection in angiogenic sprout initialisation. *J Theor Biol*, 250(1):25–36, Jan 2008. doi: 10.1016/j.jtbi.2007.09.015. URL http://dx.doi.org/10.1016/j.jtbi.2007.09.015.

[7] D. A. Beysens, G. Forgacs, and J. A. Glazier. Cell sorting is analogous to phase ordering in fluids. *PNAS*, 97:9467–71, 2000.

[8] O. Chisaka and M. R. Capecchi. Regionally restricted developmental defects resulting from targeted disruption of the mouse homeobox gene hox-1.5. *Nature*, 350(6318):473–479, Apr 1991. doi: 10.1038/350473a0. URL `http://dx.doi.org/10.1038/350473a0`.

[9] A. Czirók, K. Schlett, E. Madarász, and T. Vicsek. Exponential distribution of locomotion activity in cell cultures. *Phys. Rev. Lett.*, 81:3038 – 3041, 1998.

[10] Andras Czirok, Evan A Zamir, Andras Szabo, and Charles D Little. Multicellular sprouting during vasculogenesis. *Curr Top Dev Biol*, 81:269–289, 2008. doi: 10.1016/S0070-2153(07)81009-X. URL `http://dx.doi.org/10.1016/S0070-2153(07)81009-X`.

[11] Adriana T Dawes and Leah Edelstein-Keshet. Phosphoinositides and rho proteins spatially regulate actin polymerization to initiate and maintain directed movement in a one-dimensional model of a motile cell. *Biophys J*, 92(3):744–768, 2007. doi: 10.1529/biophysj.106.090514. URL `http://dx.doi.org/10.1529/biophysj.106.090514`.

[12] P.G. de Gennes, F. Brochard-Wyart, and D. Quere. *Capillarity and Wetting Phenomena*. Springer, New York, 2003.

[13] A. Dipasquale. Locomotion of epithelial cells. factors involved in extension of the leading edge. *Exp Cell Res*, 95(2):425–439, 1975.

[14] J. L. Doob. The brownian movement and stochastic equations. *Annals of Mathematics*, 43:351 – 369, 1942.

[15] Christopher J. Drake and Charles D. Little. *Vascular Morphogenesis: In Vivo, In Vitro, In Mente*, chapter The morphogenesis of Primordial Vascular Networks, pages 3–19. Birkhäuser Boston, 1998.

[16] D Drasdo and S Hohme. Individual-based approaches to birth and death in avascular tumors. *Math. Comput. Model.*, 37:1163–1175, 2003.

[17] Olivia du Roure, Alexandre Saez, Axel Buguin, Robert H Austin, Philippe Chavrier, Pascal Silberzan, Pascal Siberzan, and Benoit Ladoux. Force mapping in epithelial cell migration. *Proc Natl Acad Sci U S A*, 102(7):2390–2395, 2005. doi: 10.1073/pnas.0408482102. URL http://dx.doi.org/10.1073/pnas.0408482102.

[18] G A Dunn. Characterising a kinesis response: time averaged measures of cell speed and directional persistence. *Agents Actions Suppl.*, 12:14–33, 1983.

[19] G. A. Dunn and A. F. Brown. A unified approach to analysing cell motility. *J Cell Sci Suppl*, 8:81–102, 1987.

[20] Daniel A Fletcher and R. Dyche Mullins. Cell mechanics and the cytoskeleton. *Nature*, 463(7280):485–492, Jan 2010. doi: 10.1038/nature08908. URL http://dx.doi.org/10.1038/nature08908.

[21] G. Foffi, C. De Michele, F. Sciortino, and P. Tartaglia. Arrested phase separation in a short-ranged attractive colloidal system: a numerical study. *J Chem Phys*, 122(22):224903, Jun 2005. doi: 10.1063/1.1924704. URL http://dx.doi.org/10.1063/1.1924704.

[22] G. Forgacs, R. A. Foty, Y. Shafrir, and M. S. Steinberg. Viscoelastic properties of living embryonic tissues: a quantitative study. *Biophys J*, 74(5):2227–2234, 1998. doi: 10.1016/S0006-3495(98)77932-9. URL http://dx.doi.org/10.1016/S0006-3495(98)77932-9.

[23] R. A. Foty, C. M. Pfleger, G. Forgacs, and M. S. Steinberg. Surface tensions of embryonic tissues predict their mutual envelopment behavior. *Development*, 122(5):1611–1620, 1996.

[24] R.A. Foty, G. Forgacs, C.M. Pfleger, and M.S. Steinberg. Liquid properties of embryonic tissues: measurement of interfacial tensions. *Phys. Rev. Lett.*, 72:2298 – 2301, 1994.

[25] Ramsey A Foty and Malcolm S Steinberg. The differential adhesion hypothesis: a direct evaluation. *Dev Biol*, 278

(1):255–263, 2005. doi: 10.1016/j.ydbio.2004.11.012. URL http://dx.doi.org/10.1016/j.ydbio.2004.11.012.

[26] Peter Friedl. Dynamic imaging of cellular interactions with extracellular matrix. *Histochem Cell Biol*, 122:183–90, 2004.

[27] Peter Friedl and Katarina Wolf. Tube travel: the role of proteases in individual and collective cancer cell invasion. *Cancer Res*, 68 (18):7247–7249, 2008. doi: 10.1158/0008-5472.CAN-08-0784. URL http://dx.doi.org/10.1158/0008-5472.CAN-08-0784.

[28] R. Fürth. Die brownische bewegung bei berücksightigung einer persistenz der bewegungsrichtung. mit anwendungen auf die bewegung lebender infusorien. *Zeits. f. Physik*, 2:244 – 256, 1920.

[29] A. Gamba, D. Ambrosi, A. Coniglio, A. de Candia, S. Di Talia, E. Giraudo, G. Serini, L. Preziosi, and F. Bussolino. Percolation, morphogenesis, and burgers dynamics in blood vessels formation. *Phys Rev Lett*, 90 (11):118101, Mar 2003.

[30] Andrea Gamba, Antonio de Candia, Stefano Di Talia, Antonio Coniglio, Federico Bussolino, and Guido Serini. Diffusion-limited phase separation in eukaryotic chemotaxis. *Proc Natl Acad Sci U S A*, 102 (47):16927–16932, 2005. doi: 10.1073/pnas.0503974102. URL http://dx.doi.org/10.1073/pnas.0503974102.

[31] Holger Gerhardt, Matthew Golding, Marcus Fruttiger, Christiana Ruhrberg, Andrea Lundkvist, Alexandra Abramsson, Michael Jeltsch, Christopher Mitchell, Kari Alitalo, David Shima, and Christer Betsholtz. Vegf guides angiogenic sprouting utilizing endothelial tip cell filopodia. *J Cell Biol*, 161(6):1163–1177, 2003. doi: 10.1083/jcb.200302047. URL http://dx.doi.org/10.1083/jcb.200302047.

[32] J A Glazier and F Graner. Simulation of the differential adhesion driven rearrangement of biological cells. *Phys Rev E Stat Phys Plasmas Fluids Relat Interdiscip Topics*, 47(3):2128–2154, 1993.

[33] Graner and Glazier. Simulation of biological cell sorting using a two-dimensional extended potts model. *Phys Rev Lett*, 69(13):2013–2016, 1992.

[34] D.S Gray, J Tien, and C.S. Chen. Repositioning of cells by mechanotaxis on surfaces with micropatterned young's modulus. *J Biomed Mater Res A.*, 66:605–14, 2003.

[35] G Gregoire, H Chate, and Y Tu. Moving and staying together without a leader. *Physica D*, 181:157–170, 2003.

[36] Peter J M Van Haastert and Peter N Devreotes. Chemotaxis: signalling the way forward. *Nat Rev Mol Cell Biol*, 5(8):626–634, Aug 2004. doi: 1038/nrm1435. URL http://dx.doi.org/1038/nrm1435.

[37] Hisashi Haga, Chikako Irahara, Ryo Kobayashi, Toshiyuki Nakagaki, and Kazushige Kawabata. Collective movement of epithelial cells on a collagen gel substrate. *Biophysical Journal*, 88(3):2250–6, 2005. ISSN 0006-3495. doi: 10.1529/biophysj.104.047654. URL http://www.ncbi.nlm.nih.gov/pubmed/15596493. PMID: 15596493.

[38] Balázs Hegedüs, Françoise Marga, Károly Jakab, Kathy L Sharpe-Timms, and Gabor Forgacs. The interplay of cell-cell and cell-matrix interactions in the invasive properties of brain tumors. *Biophys J*, 91 (7):2708–2716, Oct 2006. doi: 10.1529/biophysj.105.077834. URL http://dx.doi.org/10.1529/biophysj.105.077834.

[39] Kelly A Hogan and Victoria L Bautch. Blood vessel patterning at the embryonic midline. *Curr Top Dev Biol*, 62: 55–85, 2004. doi: 10.1016/S0070-2153(04)62003-5. URL http://dx.doi.org/10.1016/S0070-2153(04)62003-5.

[40] Joe Howard and Anthony A Hyman. Dynamics and mechanics of the microtubule plus end. *Nature*, 422(6933): 753–758, Apr 2003. doi: 10.1038/nature01600. URL http://dx.doi.org/10.1038/nature01600.

[41] M. Shane Hutson, G. Wayne Brodland, Justina Yang, and Denis Viens. Cell sorting in three dimensions: topology, fluctuations, and fluidlike instabilities. *Phys Rev Lett*, 101(14):148105, 2008.

[42] J. A. Izaguirre, R. Chaturvedi, C. Huang, T. Cickovski, J. Coffland, G. Thomas, G. Forgacs, M. Alber, G. Hentschel, S. A. Newman, and J. A. Glazier. Compucell, a multi-model framework for simulation of morphogenesis. *Bioinformatics*, 20(7): 1129–1137, 2004. doi: 10.1093/bioinformatics/bth050. URL `http://dx.doi.org/10.1093/bioinformatics/bth050`.

[43] Lars Jakobsson, Claudio A Franco, Katie Bentley, Russell T Collins, Bas Ponsioen, Irene M Aspalter, Ian Rosewell, Marta Busse, Gavin Thurston, Alexander Medvinsky, Stefan Schulte-Merker, and Holger Gerhardt. Endothelial cells dynamically compete for the tip cell position during angiogenic sprouting. *Nat Cell Biol*, 12(10):943–953, Oct 2010. doi: 10.1038/ncb2103. URL `http://dx.doi.org/10.1038/ncb2103`.

[44] Guoying Jiang, Angela H Huang, Yunfei Cai, Monica Tanase, and Michael P Sheetz. Rigidity sensing at the leading edge through alphavbeta3 integrins and rptpalpha. *Biophys J*, 90:1804–9, 2006.

[45] E. F. Keller and L. A. Segel. Model for chemotaxis. *J Theor Biol*, 30(2): 225–234, Feb 1971.

[46] Satoru Kidoaki and Takehisa Matsuda. Shape-engineered fibroblasts: cell elasticity and actin cytoskeletal features characterized by fluorescence and atomic force microscopy. *J Biomed Mater Res A*, 81(4):803–810, 2007. doi: 10.1002/jbm.a.31114. URL `http://dx.doi.org/10.1002/jbm.a.31114`.

[47] S. Kouvroukoglou, K. C. Dee, R. Bizios, L. V. McIntire, and K. Zygourakis. Endothelial cell migration on surfaces modified with immobilized adhesive peptides. *Biomaterials*, 21(17):1725–1733, Sep 2000.

[48] D. A. Lauffenburger and A. F. Horwitz. Cell migration: a physically integrated molecular process. *Cell*, 84(3):359–369, 1996.

[49] T. Libotte, H. W. Kaiser, W. Alt, and T. Bretschneider. Polarity, protrusion-retraction dynamics and their interplay during keratinocyte cell migration. *Exp Cell Res*, 270(2):129–137, 2001. doi: 10.1006/excr.2001.5339. URL http://dx.doi.org/10.1006/excr.2001.5339.

[50] C. M. Lo, H. B. Wang, M. Dembo, and Y. L. Wang. Cell movement is guided by the rigidity of the substrate. *Biophys J*, 79 (1):144–152, 2000. doi: 10.1016/S0006-3495(00)76279-5. URL http://dx.doi.org/10.1016/S0006-3495(00)76279-5.

[51] T. Lufkin, A. Dierich, M. LeMeur, M. Mark, and P. Chambon. Disruption of the hox-1.6 homeobox gene results in defects in a region corresponding to its rostral domain of expression. *Cell*, 66(6):1105–1119, Sep 1991.

[52] G. Maheshwari and D. A. Lauffenburger. Deconstructing (and reconstructing) cell migration. *Microsc Res Tech*, 43(5):358–368, 1998. doi: 3.0.CO;2-D. URL http://dx.doi.org/3.0.CO;2-D.

[53] Carol L Manahan, Pablo A Iglesias, Yu Long, and Peter N Devreotes. Chemoattractant signaling in dictyostelium discoideum. *Annu Rev Cell Dev Biol*, 20:223–253, 2004. doi: 10.1146/annurev.cellbio.20.011303.132633. URL http://dx.doi.org/10.1146/annurev.cellbio.20.011303.132633.

[54] D. Manoussaki, S.R. Lubkin, R.B. Vernon, and J.D. Murray. A mechanical model for the formation of vascular networks in vitro. *Acta Biotheor.*, 44(3-4):271 – 282, 1996.

[55] M. Mark, T. Lufkin, J. L. Vonesch, E. Ruberte, J. C. Olivo, P. Dollé, P. Gorry, A. Lumsden, and P. Chambon. Two rhombomeres are altered in hoxa-1 mutant mice. *Development*, 119(2):319–338, Oct 1993.

[56] R. M. H. Merks. Tissue simulation toolkit, 2004. URL http://sourceforge.net/projects/tst/.

[57] R.M.H Merks, E.D. Perryn, and J.A Glazier. Contact-inhibited chemotactic motility: Role in de novo and sprouting blood vessel growth. *arXiv*, page 0505033, 2007.

[58] Roeland M H Merks, Sergey V Brodsky, Michael S Goligorksy, Stuart A Newman, and James A Glazier. Cell elongation is key to in silico replication of in vitro vasculogenesis and subsequent remodeling. *Dev Biol*, 289(1):44–54, Jan 2006. doi: 10.1016/j.ydbio.2005.10.003. URL http://dx.doi.org/10.1016/j.ydbio.2005.10.003.

[59] Roeland M H Merks, Erica D Perryn, Abbas Shirinifard, and James A Glazier. Contact-inhibited chemotaxis in de novo and sprouting blood-vessel growth. *PLoS Comput Biol*, 4(9): e1000163, 2008. doi: 10.1371/journal.pcbi.1000163. URL http://dx.doi.org/10.1371/journal.pcbi.1000163.

[60] Denise J Montell. Morphogenetic cell movements: diversity from modular mechanical properties. *Science*, 322(5907):1502–1505, 2008. doi: ence.1164073. URL http://dx.doi.org/ence.1164073.

[61] Yoichiro Mori, Alexandra Jilkine, and Leah Edelstein-Keshet. Wave-pinning and cell polarity from a bistable reaction-diffusion system. *Biophys J*, 94(9):3684–3697, May 2008. doi: 10.1529/biophysj.107.120824. URL http://dx.doi.org/10.1529/biophysj.107.120824.

[62] J. D. Murray. *Mathematical Biology*. Springer Verlag, Berlin, 2 edition, 2003.

[63] J. D. Murray, G. F. Oster, and A. K. Harris. A mechanical model for mesenchymal morphogenesis. *Journal of Mathematical Biology*, 17:125–129, 1983. ISSN 0303-6812. URL http://dx.doi.org/10.1007/BF00276117. 10.1007/BF00276117.

[64] J. D. Murray, D Manoussaki, S. R. Lubkin, and R Vernon. A mechanical theory of in vitro vascular network formation. In C. D. Little, V Mironov,

and E. H. Sage, editors, *Vascular morphogenesis: In vivo, in vitro, in mente.*, pages 223–239. Birkhauser, Boston, 1998.

[65] Patrick Namy, Jacques Ohayon, and Philippe Tracqui. Critical conditions for pattern formation and in vitro tubulogenesis driven by cellular traction fields. *J Theor Biol*, 227 (1):103–120, 2004. doi: 10.1016/j.jtbi.2003.10.015. URL http://dx.doi.org/10.1016/j.jtbi.2003.10.015.

[66] T.J. Newman. Modeling multicellular systems using subcellular elements. *Math. Biosci. Eng.*, 2:611–622, 2005.

[67] L. S. Ornstein. On the brownian motion. *Proceedings of Royal Acad. Amsterdam*, 21:96 – 108, 1919.

[68] G.F. Oster, J.D. Murray, and A.K. Harris. Mechanical aspects of mesenchymal morphogenesis. *J Embryol Exp Morphol*, 78:83–125, 1983.

[69] Noriyuki Bob Ouchi, James A. Glazier, Jean-Paul Rieu, Arpita Upadhyaya, and Yasuji Sawada. Improving the realism of the cellular potts model in simulations of biological cells. *Physica A: Statistical Mechanics and its Applications*, 329(3-4):451 – 458, 2003. ISSN 0378-4371. doi: DOI: 10.1016/S0378-4371(03)00574-0. URL http://www.sciencedirect.com/science/article/B6TVG-49D1KF5-2/2/5a4b

[70] L. Pardanaud, C. Altmann, P. Kitos, F. Dieterlen-Lievre, and C. A. Buck. Vasculogenesis in the early quail blastodisc as studied with a monoclonal antibody recognizing endothelial cells. *Development*, 100(2):339–349, Jun 1987.

[71] C. A. Parent and P. N. Devreotes. A cell's sense of direction. *Science*, 284 (5415):765–770, Apr 1999.

[72] Erica D Perryn, Andras Czirok, and Charles D Little. Vascular sprout formation entails tissue deformations and ve-cadherin-dependent cell-autonomous motility. *Dev Biol*, 313:

545–55, 2008. doi: 10.1016/j.ydbio.2007.10.036. URL http://dx.doi.org/10.1016/j.ydbio.2007.10.036.

[73] T. J. Poole and J. D. Coffin. Vasculogenesis and angiogenesis: two distinct morphogenetic mechanisms establish embryonic vascular pattern. *J Exp Zool*, 251(2):224–231, Aug 1989. doi: 10.1002/jez.1402510210. URL http://dx.doi.org/10.1002/jez.1402510210.

[74] G. Riddihough. Developmental biology. homing in on the homeobox. *Nature*, 357(6380):643–644, Jun 1992. doi: 10.1038/357643a0. URL http://dx.doi.org/10.1038/357643a0.

[75] Anne J Ridley, Martin A Schwartz, Keith Burridge, Richard A Firtel, Mark H Ginsberg, Gary Borisy, J. Thomas Parsons, and Alan Rick Horwitz. Cell migration: integrating signals from front to back. *Science*, 302(5651):1704–1709, 2003. doi: 10.1126/science.1092053. URL http://dx.doi.org/10.1126/science.1092053.

[76] J P Rieu, A Upadhyaya, J A Glazier, N B Ouchi, and Y Sawada. Diffusion and deformations of single hydra cells in cellular aggregates. *Biophys J*, 79:1903–14, 2000.

[77] Paul A Rupp, Andras Czirok, and Charles D Little. alphavbeta3 integrin-dependent endothelial cell dynamics in vivo. *Development*, 131(12):2887–97, 2004.

[78] Ravi K Sawhney and Jonathon Howard. Slow local movements of collagen fibers by fibroblasts drive the rapid global self-organization of collagen gels. *J Cell Biol*, 157(6):1083–1091, 2002. doi: 10.1083/jcb.200203069. URL http://dx.doi.org/10.1083/jcb.200203069.

[79] D Selmeczi, S Mosler, P. H. Hagedorn, N. B. Larsen, and H Flyvbjerg. Cell motility as persistent random motion: theories from experiments. *Biophys J*, 89:912–31, 2005.

[80] Sarah E Siegrist and Chris Q Doe. Microtubule-induced cortical cell polarity. *Genes Dev*, 21(5):483–496, Mar 2007. doi: 10.1101/gad.1511207. URL http://dx.doi.org/10.1101/gad.1511207.

[81] S. J. Singer and G. L. Nicolson. The fluid mosaic model of the structure of cell membranes. *Science*, 175(23):720–731, Feb 1972.

[82] J. M. Slack and D. Tannahill. Mechanism of anteroposterior axis specification in vertebrates. lessons from the amphibians. *Development*, 114(2): 285–302, Feb 1992.

[83] Supriya Srinivasan, Fei Wang, Suzana Glavas, Alexander Ott, Fred Hofmann, Klaus Aktories, Daniel Kalman, and Henry R Bourne. Rac and cdc42 play distinct roles in regulating pi(3,4,5)p3 and polarity during neutrophil chemotaxis. *J Cell Biol*, 160(3):375–385, 2003. doi: 10.1083/jcb.200208179. URL http://dx.doi.org/10.1083/jcb.200208179.

[84] M.S. Steinberg. *Cellular Membranes in Development: Proceedings, Symposium of the Society for the Study of Development and Growth*, volume 22, chapter The problem of adhesive selectivity in cellular interactions, page 321–366. Academic Press, New York, 1964.

[85] C. L. Stokes, D. A. Lauffenburger, and S. K. Williams. Migration of individual microvessel endothelial cells: stochastic model and parameter measurement. *J Cell Sci*, 99:419–30, 1991.

[86] A. Szabo and A. Czirok. The role of cell-cell adhesion in the formation of multicellular sprouts. *Math. Model. Nat. Phenom.*, 5:106–122, 2010.

[87] A. Szabo, R. Unnep, E. Mehes, W. O. Twal, W. S. Argraves, Y. Cao, and A. Czirok. Collective cell motion in endothelial monolayers. *Phys Biol*, 7(4):046007, 2010. doi: 10.1088/1478-3975/7/4/046007. URL http://dx.doi.org/10.1088/1478-3975/7/4/046007.

[88] Andras Szabo, Erica D Perryn, and Andras Czirok. Network formation of tissue cells via preferential attraction to elongated structures. *Phys Rev Lett*, 98(3):038102, 2007.

[89] Andras Szabo, Elod Mehes, Edina Kosa, and Andras Czirok. Multicellular sprouting in vitro. *Biophys J*, 95(6):2702–2710, 2008. doi: 10.1529/biophysj.108.129668. URL http://dx.doi.org/10.1529/biophysj.108.129668.

[90] B Szabo, G.J. Szollosi, B Gonci, Zs Juranyi, D Selmeczi, and T Vicsek. Phase transition in the collective migration of tissue cells: Experiment and model. *Phys. Rev. E*, 74:061908, 2006.

[91] Jessica M Teddy and Paul M Kulesa. In vivo evidence for short- and long-range cell communication in cranial neural crest cells. *Development*, 131(24):6141–6151, 2004. doi: 10.1242/dev.01534. URL http://dx.doi.org/10.1242/dev.01534.

[92] Xavier Trepat, Michael R. Wasserman, Thomas E. Angelini, Emil Millet, David A. Weitz, James P. Butler, and Jeffrey J. Fredberg. Physical forces during collective cell migration. *Nat Phys*, 5(6):426–430, June 2009. ISSN 1745-2473. URL http://dx.doi.org/10.1038/nphys1269.

[93] A. Turing. The chemical basis of morphogenesis. *Philosophical Transactions of the Royal Society of London, Series B*, 237(641):37–72, August 1952.

[94] W. O. Twal, A. Czirok, B. Hegedus, C. Knaak, M. R. Chintalapudi, H. Okagawa, Y. Sugi, and W. S. Argraves. Fibulin-1 suppression of fibronectin-regulated cell adhesion and motility. *J Cell Sci*, 114(Pt 24):4587–4598, 2001.

[95] Eleni Tzima, Mohamed Irani-Tehrani, William B Kiosses, Elizabetta Dejana, David A Schultz, Britta Engelhardt, Gaoyuan Cao, Horace DeLisser, and Martin Alexander Schwartz. A mechanosensory complex that mediates the endothelial cell response to fluid shear stress.

Nature, 437(7057):426–431, 2005. doi: 10.1038/nature03952. URL http://dx.doi.org/10.1038/nature03952.

[96] G. E. Uhlenbeck and L. S. Ornstein. On the theory of the brownian motion. *Phys. Rev.*, 36(5):823–841, Sep 1930. doi: 10.1103/PhysRev.36.823.

[97] A. Upadhyaya, J-P Rieu, J. A. Glazier, and Y. Sawada. Anomalous di usion and non-gaussian velocity distribution of hydra cells in cellular aggregates. *Physica A*, 293:549–558, 2001.

[98] Niina Veitonmaki, Jonas Fuxe, Magnus Hultdin, Geran Roos, Ralf F Pettersson, and Yihai Cao. Immortalization of bovine capillary endothelial cells by htert alone involves inactivation of endogenous p16ink4a/prb. *FASEB J*, 17(6):764–766, 2003. doi: 10.1096/fj.02-0599fje. URL http://dx.doi.org/10.1096/fj.02-0599fje.

[99] R.B. Vernon, S.L. Lara, C.J. Drake, M.L. Iruela-Arispe, J.C. Angello, C.D. Little, T.N. Wight, and E.H. Sage. Organized type I collagen influences endothelial patterns during "spontaneous angiogenesis in vitro": planar cultures as models of vascular development. *In Vitro Cell Dev Biol Anim*, 31(3):120 – 131, 1995.

[100] Tamás Vicsek, András Czirók, Eshel Ben-Jacob, Inon Cohen, and Ofer Shochet. Novel type of phase transition in a system of self-driven particles. *Phys. Rev. Lett.*, 75:1226–1229, 1995.

[101] Philip Vitorino and Tobias Meyer. Modular control of endothelial sheet migration. *Genes Dev*, 22(23):3268–3281, 2008. doi: 10.1101/gad.1725808. URL http://dx.doi.org/10.1101/gad.1725808.

[102] Fei Wang, Paul Herzmark, Orion D Weiner, Supriya Srinivasan, Guy Servant, and Henry R Bourne. Lipid products of pi(3)ks maintain persistent cell polarity and directed motility in neutrophils. *Nat Cell Biol*, 4(7):513–518, 2002. doi: 10.1038/ncb810. URL http://dx.doi.org/10.1038/ncb810.

[103] B.M. Weinstein. What guides early embryonic blood vessel formation? *Dev. Dynamics*, 215:2–11, 1999.

[104] T. Wittmann and C.M. Waterman-Storer. Cell motility: can rho GTPases and microtubules point the way? *J. Cell Sci.*, 114:3795–3803, 2001.

[105] Kenong Wu, David Gauthier, and Martin D. Levine. Live cell image segmentation. *IEEE T. Biomed. Eng.*, 42:1–11, 1995.

[106] J. Xu, Y. Tseng, and D. Wirtz. Strain hardening of actin filament networks. regulation by the dynamic cross-linking protein alpha-actinin. *J Biol Chem*, 275:35886–92, 2000.

[107] Mark Zajac, Gerald L Jones, and James A Glazier. Simulating convergent extension by way of anisotropic differential adhesion. *J Theor Biol*, 222 (2):247–259, 2003.

[108] Evan A Zamir, Andras Czirok, Brenda J Rongish, and Charles D Little. A digital image-based method for computational tissue fate mapping during early avian morphogenesis. *Ann Biomed Eng*, 33:854–65, 2005.